

ORIGINAL ARTICLE

Glutamine metabolic microenvironment drives M2 macrophage polarization to mediate trastuzumab resistance in HER2-positive gastric cancer

Xingbin Hu¹ | Zhenfeng Ma¹ | Beibei Xu¹ | Shulong Li² | Zhiqi Yao¹ |
 Bishan Liang¹ | Jiao Wang¹ | Wangjun Liao¹  | Li Lin¹ | Chunling Wang¹ |
 Siting Zheng¹ | Qijing Wu¹ | Qiong Huang¹ | Le Yu³ | Fenghua Wang⁴  |
 Min Shi¹ 

¹Department of Oncology, Nanfang Hospital, Southern Medical University, Guangzhou, Guangdong, P. R. China

²School of Biomedical Engineering, Southern Medical University, Guangzhou, Guangdong, P. R. China

³School of Pharmaceutical Sciences, Southern Medical University, Guangzhou, Guangdong, P. R. China

⁴Department of Medical Oncology, Sun Yat-sen University Cancer Center, State Key Laboratory of Oncology in South China; Collaborative Innovation Center for Cancer Medicine, Guangzhou, Guangdong, P. R. China

Correspondence

Min Shi, Department of Oncology, Nanfang Hospital, Southern Medical University, Guangzhou 510515, Guangdong, P. R. China.

Email: nfyshimin@163.com

Fenghua Wang, Department of Medical Oncology, Sun Yat-sen University Cancer Center; State Key Laboratory of Oncology in South China; Collaborative Innovation Center for Cancer Medicine, Guangzhou 510060, Guangdong, P. R. China.
 Email: wangfh@sysucc.org.cn

Abstract

Background: Trastuzumab is a first-line targeted therapy for human epidermal growth factor receptor-2 (HER2)-positive gastric cancer. However, the inevitable occurrence of acquired trastuzumab resistance limits the drug benefit, and there is currently no effective reversal measure. Existing researches on the mechanism of trastuzumab resistance mainly focused on tumor cells themselves, while the understanding of the mechanisms of environment-mediated drug resistance is relatively lacking. This study aimed to further explore the mechanisms of trastuzumab resistance to identify strategies to promote survival in these patients.

Abbreviations: HER2, human epidermal growth factor receptor 2; FBS, fetal bovine serum; DMEM, dulbecco's modified eagle's medium; GSVA, gene set variation analysis; KEGG, kyoto encyclopedia of genes and genomes; TS, trastuzumab-sensitive; TR, trastuzumab-resistant; qRT-PCR, quantitative real-time polymerase chain reaction; α -KG, α -ketoglutarate; GLUL, glutamine synthetase; SLC1A5, solute carrier family 1 member 5; SLC7A5, solute carrier family 7 member 5; GDH, glutamate dehydrogenase; GOT1, glutamic-oxaloacetic transaminase 1; GOT2, glutamic-oxaloacetic transaminase 2; GLS1, glutaminase-1; GLS2, glutaminase-2; GPT1, glutamic-pyruvic transaminase-1; GPT2, glutamic-pyruvic transaminase-2; IF, immunofluorescence; IHC, immunohistochemistry; MTT, 3-[4,5-Dimethylthiazol-2-yl]-2,5-diphenyltetrazolium bromide; Tra, trastuzumab; SD, standard deviation; CM, conditioned medium; PBMC, Peripheral blood mononuclear cell; CD31, platelet and endothelial cell adhesion molecule 1; α SMA, alpha-smooth muscle actin; Ly6G, lymphocyte antigen 6 complex locus G; NOS2, nitric oxide synthase 2; TNF- α , tumor necrosis factor alpha; IL-4, interleukin 4; ARG1, arginase 1; TGF β 1, transforming growth factor beta1; CCL22, C-C motif chemokine ligand 22; GSEA, gene set enrichment analysis; H&E, hematoxylin and eosin; TGM2, transglutaminase 2; $\text{I}\kappa\text{B}\alpha$, inhibitor kappa B alpha; M-CSF, macrophage colony-stimulating factor; SEM, scanning electron microscopy; TEM, transmission electron microscopy; CDC42, cell division cycle 42; NF- κ B, nuclear factor kappa B; IQGAP1, IQ motif containing GTPase activating protein 1; ChIP, chromatin immunoprecipitation; PMA, phorbol 12-myristate 13-acetate; Co-IP, co-immunoprecipitation; ABM, agent-based model; VEGF, vascular endothelial growth factor.

Xingbin Hu, Zhenfeng Ma, Beibei Xu contributed equally.

This is an open access article under the terms of the [Creative Commons Attribution-NonCommercial-NoDerivs](https://creativecommons.org/licenses/by-nc-nd/4.0/) License, which permits use and distribution in any medium, provided the original work is properly cited, the use is non-commercial and no modifications or adaptations are made.

© 2023 The Authors. *Cancer Communications* published by John Wiley & Sons Australia, Ltd. on behalf of Sun Yat-sen University Cancer Center.

Funding information

National Natural Science Foundation of China, Grant/Award Number: 82073325

Methods: Trastuzumab-sensitive and trastuzumab-resistant HER2-positive tumor tissues and cells were collected for transcriptome sequencing. Bioinformatics were used to analyze cell subtypes, metabolic pathways, and molecular signaling pathways. Changes in microenvironmental indicators (such as macrophage, angiogenesis, and metabolism) were verified by immunofluorescence (IF) and immunohistochemical (IHC) analyses. Finally, a multi-scale agent-based model (ABM) was constructed. The effects of combination treatment were further validated in nude mice to verify these effects predicted by the ABM.

Results: Based on transcriptome sequencing, molecular biology, and in vivo experiments, we found that the level of glutamine metabolism in trastuzumab-resistant HER2-positive cells was increased, and glutaminase 1 (GLS1) was significantly overexpressed. Meanwhile, tumor-derived GLS1 microvesicles drove M2 macrophage polarization. Furthermore, angiogenesis promoted trastuzumab resistance. IHC showed high glutamine metabolism, M2 macrophage polarization, and angiogenesis in trastuzumab-resistant HER2-positive tumor tissues from patients and nude mice. Mechanistically, the cell division cycle 42 (CDC42) promoted GLS1 expression in tumor cells by activating nuclear factor kappa-B (NF- κ B) p65 and drove GLS1 microvesicle secretion through IQ motif-containing GTPase-activating protein 1 (IQGAP1). Based on the ABM and in vivo experiments, we confirmed that the combination of anti-glutamine metabolism, anti-angiogenesis, and pro-M1 polarization therapy had the best effect in reversing trastuzumab resistance in HER2-positive gastric cancer.

Conclusions: This study revealed that tumor cells secrete GLS1 microvesicles via CDC42 to promote glutamine metabolism, M2 macrophage polarization, and pro-angiogenic function of macrophages, leading to acquired trastuzumab resistance in HER2-positive gastric cancer. A combination of anti-glutamine metabolism, anti-angiogenesis, and pro-M1 polarization therapy may provide a new insight into reversing trastuzumab resistance.

KEYWORDS

Gastric cancer, glutamine metabolism, macrophage, mathematical model, microvesicles, trastuzumab

1 | BACKGROUND

Gastric cancer is one of the most common malignant tumors worldwide. In China, over 70% of the patients are diagnosed at an advanced stage, and approximately 20% of the patients with advanced gastric cancer are human epidermal growth factor receptor-2 (HER2)-positive [1, 2]. These patients generally have a poor prognosis and a high recurrence rate [3]. Trastuzumab is a humanized monoclonal antibody targeting HER2. In 2010, the trastuzumab for gastric cancer trial found that trastuzumab combined with chemotherapy could significantly improve the survival of patients with advanced HER2-positive gastric

cancer, which established the status of trastuzumab as the first-line treatment of HER2-positive gastric cancer and opened a new era of targeted therapy for gastric cancer [4]. In the following decade, many targeted therapies for gastric cancer, including new drugs targeting HER2 (such as lapatinib and trastuzumab emtansine), mammalian target of rapamycin (mTOR) inhibitors, and c-Met receptor tyrosine kinase inhibitors have undergone clinical trials but all have ultimately failed to obtain positive results [5, 6]. Trastuzumab remains the only first-line targeted therapy for HER2-positive gastric cancer. However, most patients develop acquired resistance within 1 year of continuous trastuzumab treatment [7]. Therefore, there is an urgent

need to identify the mechanism of acquired trastuzumab resistance and propose targeted strategies to improve the survival of HER2-positive gastric cancer patients.

Although a variety of acquired trastuzumab resistance mechanisms have been discovered in preclinical studies [5, 8, 9], there is no effective treatment for overcoming trastuzumab resistance. Currently, trastuzumab resistance mechanisms mainly focus on intrinsic characteristics of tumor cells, such as the activation of the bypass pathway (insulin-like growth factor 1 receptor, HER3, and so on) and the upregulation of downstream signaling pathways [9, 10]. However, in addition to their inherent characteristics, tumor cells also exist in a complex microenvironment. Metabolic processes in the microenvironment change constantly and dynamically. Different metabolic patterns affect the differentiation of different immune cell subsets, causing the entire microenvironment to evolve in the direction of tumor promotion [11, 12]. Therefore, metabolic reprogramming is a cancer feature associated with acquired trastuzumab resistance.

Previous studies have found that hexokinase 2 and lactate dehydrogenase A expression promote trastuzumab resistance by upregulating glycolysis [13, 14]. The mevalonate metabolic pathway promotes trastuzumab resistance through mTOR signaling [15]. However, there are few studies on the relationship between trastuzumab resistance and amino acid metabolism, particularly glutamine metabolism. A previous study suggested that glutamine metabolism in tumor cells activates adenosine 5'-monophosphate-activated protein kinase (AMPK)-protein Kinase B (AKT) signaling to promote metformin resistance [16]. Glutamine can also affect drug resistance in tumor cells through metabolic enzymes such as glutaminase 1 (GLS1) and glutamate dehydrogenase (GDH) [17]. In addition, a study on breast cancer showed that tumor-associated fibroblasts can produce and secrete glutamine, which enters the microenvironment to promote the energy metabolism of tumor cells, leading to tamoxifen resistance [18]. HER2-positive breast cancer has a higher glutamine metabolic activity [19]. Therefore, we hypothesized that glutamine metabolism is associated with trastuzumab resistance. First-generation inhibitors of glutamine metabolism were developed as early as the 1980s, and the latest inhibitor, telaglenastat (CB839), has undergone several clinical studies [20–22]. Therefore, targeting glutamine metabolism may be an effective strategy to reverse trastuzumab resistance.

Macrophages, including pro-inflammatory M1 and anti-inflammatory M2 macrophages, are important components of the tumor microenvironment. There are significant differences in the metabolism of M1 and M2 macrophages [23]. A previous study revealed that tumor cells can influence the phenotype and function

of macrophages through metabolic products, metabolic enzymes, and exosomes [24]. It has been found that tumor cell-derived succinic acid regulates downstream signaling pathways to promote polarization of macrophages by activating succinic acid receptors on the surface of macrophages [25]. Tumor-derived exosomes activate signaling pathways in macrophages to promote macrophage polarization [26]. Thus, it is possible that tumor cells influence the phenotype of macrophages by regulating glutamine metabolism, thereby mediating trastuzumab resistance.

Extracellular vesicles, including microvesicles and exosomes, can act as mediators in the interaction between tumor cells and macrophages. Microvesicles, which are greater than 100 nm in diameter and formed directly from shedding of the plasma membrane, can encapsulate and deliver metabolic substrates, products, key enzymes, and RNA to facilitate cell interactions [27, 28]. Recent studies have suggested that microvesicles shed from tumor cells may contain glutaminase GLS1 [20, 28, 29]. Therefore, we speculated that GLS1 microvesicle transmission mediates metabolic interactions between tumor cells and macrophages and induces trastuzumab resistance.

In this study, we investigated the metabolic interaction between tumor cells and macrophages mediating trastuzumab resistance, and explored the role of combination therapy in reversing trastuzumab resistance using mathematical models and animal experiments.

2 | MATERIALS AND METHODS

2.1 | Patients

The patients included in this study were diagnosed with HER2-positive gastric cancer and received trastuzumab treatment at Nanfang Hospital (Guangzhou, Guangdong, China) and Sun Yat-sen University Cancer Center (Guangzhou, Guangdong, China) between 2013 and 2020. Immunohistochemistry (IHC) test and fluorescence in situ hybridization (FISH) test were used to test HER2 expression and gene amplification levels of these patients, respectively. According to American Society of Clinical Oncology-College of American Pathologists (ASCO-CAP) guidelines [30], HER2 positivity was defined as IHC scores of 3+ or IHC scores of 2+ with FISH-positive findings. According to the Response Evaluation Criteria in Solid Tumors (RECIST 1.1) [31], the patients with complete response or partial response were defined as trastuzumab-sensitive, and those with progressive disease were defined as trastuzumab-resistant. Trastuzumab-sensitive tumor samples were collected from first-consultation patients assessed with complete response or partial response

at first assessment after trastuzumab treatment, and trastuzumab-resistant tumor samples were collected after the patients were assessed for disease progression. The blood samples from patients were collected at the time of therapeutic assessment. Signed informed consent was obtained from all the patients for the use of their clinical information and tumor samples. All research procedures were approved by the Nanfang Hospital Ethics Review Board and conformed to the International Ethical Guidelines for Biomedical Research Involving Human Subjects.

2.2 | Cell lines, cell culture, and establishment of trastuzumab-resistant cells

The human HER2-positive gastric cancer cell lines NCI-N87 and SNU216 were used in this study. NCI-N87 cells (RRID: CVCL_IL03) were obtained from the National Collection of Authenticated Cell Cultures (NCACC, Shanghai, China), and SNU216 cells (RRID: CVCL_3946) were a gift from Dr. Rui-Hua Xu (Sun Yat-sen University Cancer Center). The procedure for creating trastuzumab-resistant cells was described in our previous study [14]. Briefly, trastuzumab-sensitive, parental NCI-N87 and SNU216 cells were used to establish trastuzumab-resistant cells by a three-dimensional (3D) collagen model. A 3D model was set up using three collagen layers (400 μ L; 2052954, Gibco, Carlsbad, CA, USA) in 12-well culture dishes, where the middle layers contained NCI-N87 or SNU216 single cell suspension (5,000 cells). A RPMI-1640 medium (31800, Solarbio, Beijing, China) supplemented with 10% fetal bovine serum (FBS; S9030, Solarbio) and trastuzumab (10 μ g/mL, Roche, Basel, Switzerland) was added and replaced every 3 days. After 6 months, trastuzumab-resistant NCI-N87 cell (NCI-N87-TR) and trastuzumab-resistant SNU216 cell (SNU216-TR) were established and detected using a cell ability assay. The authenticity of the four cell lines NCI-N87, NCI-N87-TR, SNU216, and SNU216-TR was confirmed using short tandem repeat analysis. The human monocytic cell line THP-1 was obtained from the NCACC. THP-1 monocytes were incubated with phorbol 12-myristate 13-acetate (PMA; 100 ng/mL; S7791, Selleck, Houston, TX, USA), a phorbol ester, for 48 h to differentiate into macrophages. All these cells were cultured in complete RPMI-1640 or Dulbecco's Modified Eagle Medium (DMEM) (12100, Solarbio) supplemented with 10% FBS. All cells were tested regularly for mycoplasma contamination and were cultured in a 5% CO₂ incubator at 37°C. All experiments were performed within 3-8 passages after thawing the cells. The parental and trastuzumab-resistant cell lines were authenticated using short tandem repeat sequencing.

Bis-2-(5-phenylquinoxalino-1,2,4-thiadiazol-2-yl)ethyl sulfide (BPTES; S6951, Selleck) and CB839 (S7655, Selleck) were used as GLS1 inhibitors at a concentration of 20 μ mol/L in tumor cell proliferation and apoptosis assays; ZCL278 (10 μ mol/L; S7293, Selleck) was used to inhibit cell division cycle 42 (CDC42)-GTP in the validation of the CDC42-NF- κ B p65 pathway and microvesicle secretion. PMA (50 nmol/L) was used as nuclear factor kappa-B (NF- κ B) agonist in rescue experiment of validation of the CDC42-NF- κ B p65 pathway.

2.3 | Transcriptome sequencing

Total RNA was isolated from trastuzumab-sensitive and trastuzumab-resistant cells/tissues by TruSeq RNA Sample Preparation Kit (Illumina, San Diego, CA, USA). The sequencing library of each sample was constructed using the Ion Proton Total RNA-Seq Kit version 2 (4479789, Thermo Fisher, Carlsbad, CA, USA) based on the protocol. RNA-seq was performed by BGISEQ-500 sequencing platform (BGI, Shenzhen, Guangdong, China)

2.4 | Bioinformatic analysis

2.4.1 | Initial processing of transcriptome data

Transcripts per kilobase million (TPM) values were used, unless specified. The expression matrix was divided into trastuzumab-sensitive group and trastuzumab-resistance group according to clinical information.

2.4.2 | Calculation of metabolism characteristics score

The metabolic pathways were downloaded from the Kyoto Encyclopedia of Genes and Genomes (KEGG) database (<https://www.genome.jp/kegg/>) [32]. A total of 1,655 human metabolic genes from 84 metabolic pathways were obtained [33]. Pathways were clustered into 11 major categories based upon KEGG classifications. Except that, we got glutamine metabolism gene set from gene set enrichment analysis (GSEA) database (<http://www.gsea-msigdb.org/gsea/msigdb/index.jsp/>) by C2 (curated gene sets) data channel. Gene set variation analysis (GSVA) [34] was utilized to calculate the enrichment score of each metabolic pathway in each sample with transcriptomic data. Metabolism pathway scores (trastuzumab-resistant subtype vs. trastuzumab-sensitive subtype) were compared using the Limma R package [35]. Log₂ (fold change) > 0.4

and false discovery rate (FDR) < 0.05 were considered significant upregulation.

2.4.3 | GSEA

Pathways including glutamine metabolism, angiogenesis, and extracellular vesicles gene set were obtained from the GSEA database by C2 and C5 (ontology gene sets) data channels. Metabolism pathway scores (trastuzumab-resistant subtype vs. trastuzumab-sensitive subtype) were compared using the Limma R package with the standard \log_2 (fold change) = 1 and FDR = 0.05. GSEA function and Gseaplot2 function were used for enrichment analysis under ClusterProfiler R package [36].

2.4.4 | Immune infiltration score

Twenty-two types of tumor-infiltrating lymphocytes were identified based on CIBERSORT, a gene expression-based deconvolution algorithm that uses a set of barcoded gene expression values (a “signature matrix” of 547 genes) to characterize immune cell composition [37, 38]. Only cases with CIBERSORT $P < 0.05$ were included in subsequent analyses. Enrichment levels of the 29 immune signatures in each sample were quantified by single-sample gene-set enrichment analysis (ssGSEA).

2.5 | Quantitative real-time PCR (qRT-PCR) assay

According to the manufacturer’s instructions, total RNA were extracted from tumor cells and macrophages with TRIzol reagent (10296010, Invitrogen, Carlsbad, CA, USA) and reversely transcribed into cDNA using the reverse transcription kit HiScript II Q RT SuperMix for qPCR (R222-01, Vazyme, Nanjing, Jiangsu, China). qRT-PCR was performed using the QuantStudio 6 Pro Real-Time PCR System (Thermo Fisher). The program for amplification was one cycle of 95°C for 3 min, followed by 39 cycles of 95°C for 10 s and 55°C for 30 s. The indicator gene expression was scaled using β -actin expression as control. The $2^{-\Delta\Delta C_t}$ method was used to calculate the expression fold change. The primers used are shown in Supplementary Table S1.

2.6 | Western blotting (WB)

WB was performed as previously described [14]. Briefly, 30 μ g of protein was loaded and separated by sodium

dodecyl sulfate-polyacrylamide gel electrophoresis (SDS-PAGE) under reducing conditions and then transferred to polyvinylidene fluoride membranes (Merck Millipore, Boston, MA, USA). Membranes were blocked with 5% skimmed milk or bovine serum albumin (Fude, Hangzhou, Zhejiang, China) for 1 h and incubated with the indicated antibody at 4°C overnight. After incubating the bands with horseradish peroxidase-conjugated secondary antibody (FDM007 and FDR007, Fude) for 1 h at 20°C–30°C, immunoblots were visualized using a chemiluminescence detection system (Tanon, Shanghai, China). Antibodies for WB: anti-nuclear factor kappa-B (NF- κ B) p65 (1:1,000; Cat#8242S), anti-phospho-NF- κ B p65 (1:1,000; Cat#3033S), anti-IQ motif-containing GTPase-activating protein 1 (IQGAP1; Cat#20648S) were obtained from Cell Signaling Technology (Beverly, MA, USA); anti-glutaminase C (GAC; 1:1,000; 19958-1-AP), anti-kidney glutaminase (KGA)/GAC (1:5,000; 66265-1-Ig), anti-IQGAP1 (1:4,000; 22167-1-AP), anti-transglutaminase 2 (TGM2; 1:2,000; 15100-1-AP), anti-Alix (1:5,000; 12422-1-AP), anti-Flotillin 2 (1:1,000, 28208-1-AP), anti-NF- κ B inhibitor (I κ B) alpha (1:5,000; 10268-1-AP), anti- β -actin (1:5,000, 66009-1-Ig), anti-glyceraldehyde-3-phosphate dehydrogenase (GAPDH; 1:5,000; 60004-1-Ig), anti-Histone-H3 (1:4,000; 17168-1-AP) were obtained from Proteintech (Rosemont, IL, USA); anti-CDC42 (1:500; WL01165) was obtained from Wanleibio (Shenyang, Liaoning, China); anti-CDC42-GTP (1:500; Cat#26905) was obtained from NewEast Biosciences (King of Prussia, PA, USA).

2.7 | Animals

Female BALB/c nude mice (6–8 weeks old, 17–20 g) were obtained from the Experimental Animal Center of Nanfang Hospital. For tumor formation, 1×10^6 NCI-N87 and NCI-N87-TR cells were injected into the left and right flanks of nude mice, respectively. Tumor size was measured every alternate day using calipers. The tumor volume (mm^3) was calculated using the following formula: tumor volume = $0.5 \times L \times W^2$, where V is the volume, L is the length, and W is the width. Seven days after tumor implantation, the mice were randomly divided into six experimental groups (5–8 mice per group): trastuzumab-sensitive + phosphate-buffered saline (PBS; BL601A, Biosharp, Hefei, Anhui, China); trastuzumab-sensitive + trastuzumab; trastuzumab-resistant + PBS; trastuzumab-resistant + trastuzumab; trastuzumab-resistant + BPTES; trastuzumab-resistant + trastuzumab + BPTES. The following 4-week treatments were given as one or as a combination of the following: PBS, 100 μ L per mice, intraperitoneal injection, twice a week; trastuzumab,

20 mg/kg, intraperitoneal injection, twice a week; BPTES, 12.5 mg/kg, intraperitoneal injection, twice a week. All animal procedures were performed under the supervision of the Nanfang Hospital Animal Care and Use Committee (Application No.: NFYY-2021-0516), and all mice were housed at 23-25°C at the Experimental Animal Center of Nanfang Hospital. Standard rodent laboratory diet and water were provided adequately and regularly. Tumor volumes and weights were measured and recorded. Based on the animal use protocol, all mice that had completed experimental tasks or in a moribund state were humanely euthanized by cervical dislocation after deep anesthesia. Two criteria to identify the moribund mice: (1) mice that showed signs of disease-like difficulty of breathing, eating, or drinking; (2) a mouse loses $\geq 15\%$ body weight in 4 days.

2.8 | Immunofluorescence (IF) staining

NCI-N87, NCI-N87-TR, SNU216, SNU216-TR cells, and subcutaneous tumor tissues of xenograft nude mice were fixed with 4% paraformaldehyde (DF0135, Leagene, Beijing, China) and then permeabilized with PBS containing 0.1% Triton X-100 (AR-0341, Dinguocs, Beijing, China). The samples were then incubated with primary antibodies anti-GLS1 (1:500; 66265-1-Ig, Proteintech), anti-F4/80 (1:1,000; 29414-1-AP, Proteintech), anti-CD31 (1:100; 11265-1-AP, Proteintech), anti-CD206 (1:200; 60143-1-Ig, Proteintech), anti-TGM2 (1:200; 15100-1-AP, Proteintech), and anti-Flotillin 2 (1:100; 28208-1-AP, Proteintech) overnight at 4°C. Next, the cells or tissues were incubated with the secondary antibodies Alexa Fluor 555-labeled donkey anti-mouse IgG (1:200; Beyotime, Shanghai, China) and Alexa Fluor 488-labeled goat anti-rabbit IgG (1:200; Beyotime) for 1 h at 20°C-30°C. Finally, the cells or tissues were incubated for 10 min with 4',6-diamidino-2-phenylindole (DAPI; 1:800; Beyotime) diluted with methanol (GHTECH, Shantou, Guangdong, China) in 50 μ L for each sample to stain the nucleus. Fluorescent microscopic images were captured and processed using a laser confocal microscope (A1-DUVB-2, Nikon, Tokyo, Japan).

2.9 | Detection of GLS1 enzyme activity, α -Ketoglutarate (α -KG) content and glutamine content

The following kits were used to detect GLS1 enzyme activity, α -KG content and glutamine content of cells and tissues respectively: the GLS1 activity test kit (BC1455, Solarbio), the α -KG enzyme-linked immunosorbent assay (ELISA)

Kit (2M-KMLJM220809m and 2H-KMLJh313735, Camilo Biological, Nanjing, Jiangsu, China) and the glutamic acid (Glu) content detection kit (BC1580, Solarbio). All experimental procedures followed the instructions of the kits.

2.10 | MTT assay

Cells were plated in 96-well plates at 2×10^3 cells/well, and exposed to trastuzumab (10 μ g/mL), BPTES (20 μ mol/L) or CB839 (20 μ mol/L) for 48 h. Thiazolyl blue (3-(4,5-dimethyl-2-thiazolyl)-2,5-diphenyltetrazolium bromide (MTT; ST316, Beyotime) was added to the cells to incubate for 4-6 h, then, 150 μ L of dimethyl sulfoxide (D806645, Macklin, Shanghai, China) was added to each well, and the plate was well oscillated. Absorbance was measured at 570 nm using the SpectraMax M5 microplate reader (Molecular Devices, San Jose, CA, USA). Each assay was replicated three times.

2.11 | ANNEXIN V-fluorescein isothiocyanate (FITC)/propidium iodide (PI) and 7-aminoactinomycin D (7-AAD)/allophycocyanin (APC) apoptosis detection

The cells were analyzed with a flow cytometer-BD FACS Melody (BD Bioscience, Franklin Lake, NJ, USA). ANNEXIN V- FITC/PI Apoptosis Detection Kit (CA1020, Solarbio) and Annexin V-APC/7-AAD Apoptosis kit (AP105, Multi Sciences, Hangzhou, Zhejiang, China) were used to divide cells into viable cells, dead cells, early apoptotic cells, and late apoptotic cells. The relative proportions of early apoptotic cells and late apoptosis cells were recorded. The data were analyzed with FlowJo-V10 CL software (Tree Star, Ashland, OR, USA). Each assay was replicated three times.

2.12 | Hematoxylin-eosin (H&E) staining

Organs (the heart, liver, spleen, lung and kidney) of xenograft nude mice were fixed in 4% formaldehyde overnight and embedded in paraffin (8002-74-2, Merck Millipore). The sections (4 μ m) were stained with H&E (DH0006, Leagene) to examine morphology. The pathological diagnosis was performed jointly by two trained pathologists. Whole slice sections were imaged and scanned using the Slide Scan System SQS-120P (Shengqiang, Shenzhen, Guangdong, China).

2.13 | IHC staining

Tumor tissue from trastuzumab-sensitive and trastuzumab-resistant patients and xenograft nude mice were fixed in 4% formaldehyde overnight and embedded in paraffin. Serial sections (4 μm) were incubated with horseradish peroxidase-labeled Polymer anti-rabbit or anti-mouse antibody and 3,3'-diaminobenzidine from DAKO (Copenhagen, Denmark). IHC staining was used to detect the expression levels of GLS1 (1:500; 66265-1-Ig, Proteintech), F4/80 (1:1,000; 29414-1-AP, Proteintech), CD206 (1:10,000; 60143-1-Ig, Proteintech), lymphocyte antigen 6 complex locus G6D (Ly6G; 1:2,000; ab238132, Abcam, Cambridge, UK), CD31 (1:1,000; 11265-1-AP, Proteintech), CD68 (1:1,000; ab201340, Abcam), CD11c (1:500; 17342-1-AP, Proteintech) and alpha-smooth muscle actin (αSMA ; 1:200; 55135-1-AP, Proteintech). Images were obtained using the Slide Scan System SQS-120P.

2.14 | Transfection

The human GLS1 gene (GenBank accession number 2744) and IQGAP1 gene (GenBank accession number 8826) were cloned by OriGene Technologies Inc (Rockville, Rockwell, MD, USA). siGLS1 was achieved by using the Lipofectamine 2000 Kit (11668019, Invitrogen). Plasmids of shIQGAP1 and shGLS1 (pMD2.0G and psPAX) were purchased from Genechem Company (Montreal, QU, Canada). Plasmid of CDC42-WT, CDC42-G12V, and CDC42-T17N were purchased from GeneCopoeia Company (Guangzhou, Guangdong, China). NCI-N87-TR and SNU216-TR cells were infected with lentivirus carrying corresponding plasmid, respectively, and selected with 1 $\mu\text{g}/\text{mL}$ puromycin medium (A1113803, Invitrogen). The gene or amino acid sequences are listed in Supplementary Tables S2-S3.

2.15 | Preparation and polarization of peripheral blood mononuclear cells (PBMCs)

Whole-blood samples were collected from 20 healthy volunteers (20 mL per person), and the human peripheral blood monocyte isolation kit (P8680, Solarbio) was used to separate monocytes. Monocytes were seeded in 12-well plates (approximately 2×10^5 cells per well) and incubated in DMEM supplemented with 10% FBS. Monocytes were polarized with macrophage colony-stimulating factor (M-CSF) (10 ng/mL, 11792-HNAH-B, Sinobiological, Houston, TX, USA) for 7 days. After culturing for the indicated times, the macrophages were harvested for subsequent experi-

ments. The purity of macrophages was confirmed by flow cytometry. The data were analyzed using FlowJo-V10 CL software.

2.16 | Co-culture system for tumor cells and macrophages

In the co-culture model, tumor cells (parental and trastuzumab-resistant NCI-N87 and SNU216 cells) and macrophages (THP-1 and PBMC) were cultured in a chamber (JET Biofil, Guangzhou, Guangdong, China). A total of 2×10^5 tumor cells were added to the upper layer, and 2×10^5 macrophages were cultured in the lower layer, or in the contrary. Co-cultivation lasted for 48 h. The following reagents were added to tumor cells as indicated: BPTES (20 $\mu\text{mol}/\text{L}$), CB839 (20 $\mu\text{mol}/\text{L}$), GW4869 (10 $\mu\text{mol}/\text{L}$, S7609, Selleck). The lower layer of cells was collected for protein and RNA extraction, and M1 and M2 phenotype polarization indicators were detected via qRT-PCR and flow cytometry.

2.17 | Macrophage polarization assay

Macrophage polarization was detected by flow cytometry. Briefly, cells were incubated with the antibody conjugated with fluorescence in 100 μL of flow cytometry staining buffer (S1001, Multi Sciences) and were protected from light and incubated for 30 min at 20°C-30°C. The data were analyzed with FlowJo-V10 CL software. Each assay was replicated three times. Antibodies for flow cytometry: anti-human CD86 (Cat#305419), anti-human CD163 (Cat#333603), anti-human CD14 (Cat#301803) were purchased from Biolegend (San Diego, CA, USA); anti-mouse CD206 (Product#12-2061-80) was purchased from Invitrogen; anti-mouse CD11c (70-AM011C05-100) and anti-mouse F4/80 (AM04800201) were purchased from Multi Sciences.

2.18 | Chorioallantoic membrane vascular assay

Chorioallantoic membrane vascular assay used in this study was previously described by Donahue et al. [39] and Merckx et al. [40]. Briefly, fertilized, white Leghorn eggs (Xinxingdahua, Yunfu, Guangdong, China) were placed in the incubator and incubated for 10 days at $37.8 \pm 0.5^\circ\text{C}$ and 40%-60% humidity. On day 10 of incubation, viable eggs were selected for dosing. A rectangular window was cut using a dremel drill, and a polytetrafluoroethylene resin ring was placed on the intact chorioallantoic membrane of

chicken embryo with tweezers as the test and observation area. In the supernatant of macrophages in the co-culture system, interleukin (IL)-4 (10 ng/mL, Pepro Tech, Cranberry, NJ, USA) and BPTES (20 μ mol/L) were added into the test ring as indicated, and the opening was then sealed with transparent tape. The eggs were then put back to the incubator for further cultivation until 48 h. The test ring was removed, and the overall blood vessel growth of the chicken embryo was observed, using a camera to shoot.

2.19 | Isolation of microvesicles

NCI-N87, NCI-N87-TR, SNU216 and SNU216-TR cells were cultured with FBS-free medium for 12 h after the corresponding treatments. Conditioned medium from at least 2×10^7 cells of various types were collected. Next, 100 mL supernatant of each sample was centrifugated to isolate microvesicles in three steps as previously reported [41]. In brief, the cell supernatant was centrifugated at $1,000 \times g$ (5 min, 4°C), then at $10,000 \times g$ (30 min, 4°C) to discard dead cells and cellular debris, and finally at $100,000 \times g$ (2 h, 4°C) by Ultracentrifuge (Beckman Coulter, Bria, CA, USA). After centrifugation, the microvesicles was finally resuspended in 400 μ L of PBS for subsequent experiments. The protein concentration of microvesicles was measured with a BCA Protein Assay Kit (PC0020, Solarbio) according to the manufacturer's protocols. The morphology of microvesicles was observed by transmission electron microscope (TEM).

2.20 | TEM and scanning electron microscope (SEM)

For TEM, the H-7000FA scanning transmission electron microscope (HITACHI, Tokyo, Japan) was used to image microvesicles, which were extracted from parental and trastuzumab-resistant NCI-N87 and SNU216 cells. Briefly, microvesicles was resuspended in PBS, stored at 4°C, and negative staining was completed within 2 h. For SEM, log-phase parental and trastuzumab-resistant NCI-N87 and SNU216 cells were collected from 12-well plates, and then fixed with 2.5% glutaraldehyde (Phygene, Fuzhou, Fujian, China) at 4°C and rinsed with PBS thrice. After fixing in 1% osmium tetroxide (Electron Microscopy Sciences, Hatfield, PA, USA), these samples were dehydrated through an ascending ethanol gradient and dried with hexamethyldisilazane (Zrbiorise, Shanghai, China). Finally, the samples were sputtered with gold-palladium and observed under the scanning electron microscope (JSM-7900F, Tokyo, Japan).

2.21 | Nuclear and cytoplasmic protein extraction

Cells were washed and harvested in cold PBS. The cytoplasmic and nuclear fractions were then separated by using a Nuclear and Cytoplasmic Protein Extraction Kit (P0027, Beyotime) according to manufacturer's recommended procedures. Protein concentrations were determined by using BCA protein assay kit according to the manufacturer's protocols, and then subjected to WB.

2.22 | Chromatin immunoprecipitation (ChIP) assay

ChIP assay was performed using a SimpleChIP Enzymatic Chromatin IP kit (Cat#9003, Cell Signaling Technology) following the product instructions. The fragmented chromatin was incubated with rabbit monoclonal anti-NF- κ B p65 (1:100), rabbit anti-histone 3, and rabbit anti-IgG (for the negative control) antibodies overnight at 4°C. Target-bound DNA fragments were reversely crosslinked and purified, then amplified by qRT-PCR. Primer pairs for the ChIP assay are listed in Supplementary Table S4.

2.23 | Co-immunoprecipitation (Co-IP) assays

A total of 1×10^7 NCI-N87-TR and SNU216-TR cells were collected. Next, cell lysates were incubated with primary anti-GAC (1:400; 19958-1-AP, Proteintech) or anti-IQGAP1 antibody (1:200; 22167-1-AP, Proteintech), and mixed with protein A/G-Sepharose beads (P001-2, 7 Sea Biotech, Shanghai, China) overnight at 4°C. After extensive washing with PBS, the beads were boiled in $5 \times$ SDS-PAGE loading buffer (FD006, Fude) for 10 min and analyzed by WB with specific antibodies to detect the protein complex.

2.24 | Agent-based model (ABM)

The ABM is a computational model used to simulate the actions and interactions of autonomous conscious agents, evaluating the role of agents in the system as a whole through image presentation. The efficacy of drugs can be predicted and evaluated by constructing multi-scale mathematical models including molecular scale, cellular scale, microenvironment scale and tissue scale. These four scales describe the dynamic changes of signaling pathways, cells, metabolism and blood vessels in the microenvironment,

which are described in details below. The ABM is a tool that can play an important role in the current study of tumor microenvironment [42, 43]. The ABM was applied through the MATLAB software (MathWorks, Natick, MA, USA). The process and equations used in this study are as follows. Coefficients of the equations are detailed in the Supplementary Tables S5-S13. The whole model was simulated on the lattice of 200×200 , which represented the tumor section of approximately 5 mm. The lattice spacing was $20 \mu\text{m}$, which was about the diameter of tumor cells.

2.24.1 | Model initialization

MATLAB realizes the simulation of initial value using Gaussian distribution to determine the initial concentration distribution of substances on the cell, microenvironment and molecular scale. The meanings and values of the coefficients in these equations are in Supplementary Table S5.

In the microenvironment of the entire model area [$0 \sim 1$, $0 \sim 1$]:

$$XG = Ga + (Gm - Ga) \times e^{\frac{-2x^2}{\text{sigamag}^2}}$$

$$O2 = Ka + (Km - Ka) \times e^{\frac{-2x^2}{\text{sigamao}^2}}$$

$$Tra = Traa + (Tram - Traa) \times e^{\frac{-2x^2}{\text{sigamatra}^2}}$$

$$f = 0.75 \times e^{\frac{-x^2}{0.45}}$$

In the area of the circular model with a center (0.5, 0.75) and a radius of 0.02:

80% of the area was randomly distributed with tumor cells.

$$EGF = Tm \times e^{\frac{-2[(yy - 0.75)^2 + (xx - 0.5)^2]}{\text{sigamat}^2}}$$

$$AKG = akga \times e^{\frac{-2[(yy - 0.75)^2 + (xx - 0.5)^2]}{\text{sigamaakg}^2}}$$

In the area of the circular model with a center (0.5, 0.75) and a radius of 0.05:

80% of the area was randomly distributed with M1 cells.

$$NO = na \times e^{\frac{-2[(yy - 0.75)^2 + (xx - 0.5)^2]}{\text{sigaman}^2}}$$

In the area of the circular model with a center (0.5, 0.75) and a radius of 0.24:

85% of the area was randomly distributed with M0 cells.

$$IL - 6 = Ka6 + (Km6 - Ka6) \times e^{\frac{-2[(yy - 0.75)^2 + (xx - 0.5)^2]}{\text{sigma6}^2}}$$

$$IL - 10 = Ka10 + (Km10 - Ka10)$$

$$\times e^{\frac{-2[(yy - 0.75)^2 + (xx - 0.5)^2]}{\text{sigma10}^2}}$$

The initial distribution of blood vessels at the tissue scale was as follows.

It was assumed that the initial blood vessels are distributed in the area of $y = 0.2$, and the endothelial cells of the root tips of the initial sprouting vessels are distributed at (0.1, 0.2), (0.3, 0.2), (0.4, 0.2), (0.5, 0.2), (0.6, 0.2), (0.7, 0.2) and (0.9, 0.2).

2.24.2 | Molecular scale

This scale includes the HER2 signaling pathway and downstream cell cycle pathway (Supplementary Figure S1A). It is mainly described by enzymatic reaction equation, which determines the concentration of Phospholipase C (PLC) γ and affects the phenotype of tumor cells. V represents production and consumption rate. Supplementary Tables S6-S8 show the concentration of each component (Supplementary Figure S1A) in the HER2 signaling are described by a system of coupled ordinary differential equations (ODEs). Where V denotes Xi productivity and consumption rate. The coefficients of ODEs are in Supplementary Tables S9-S10.

2.24.3 | Cellular scale

The cell scale mainly includes proliferation, migration and phenotypic transformation of tumor cells and macrophages (Supplementary Figure S1B).

Tumor cell proliferation: According to the concentration of glucose in different parts of the tumor, the tumor was divided into necrotic region, resting region and activation region. When the glucose concentration is lower than a certain threshold or the nitric oxide (NO) is higher than a certain threshold, we define it as a necrotic area [44] (Supplementary Figure S1C). The necrotic region was defined as the region with insufficient glucose levels for viability or sufficient NO levels for killing tumor. The resting region was defined as the region in which glucose

levels were sufficient for viability but not proliferation. The activation region was defined as the region with sufficient glucose levels for proliferation. The tumor cells in the activation region activated the HER2 and downstream cellular pathways to promote the proliferation of tumor cells. Tumor growth is achieved through progress at the molecular scale. Macrophage polarization: the macrophages come from differentiation of monocytes transported from blood vessels or macrophages originally retained in tumor tissue. It was assumed that the intensity coefficient is K . $KM1/KM2$ denotes intensity of polarization from M0 to M1/M2 under natural conditions. $KAKG$ represents the intensity of polarization of M1 to M2 by α -KG. $KM12$ represents the intensity of polarization from M1 to M2 under natural conditions. $CM1F/(CM2F, CAKG)$ is the local concentration of cytokines and other factors conducive to M1 and M2 polarization, which are released from living (proliferative or anoxic) tumor cells. We assumed that the possibility of M2 polarizing to M1 was extremely low. In this study, the polarization from M1 to M2 was assumed to be unidirectional. The coefficients are in Supplementary Table S11.

The original position is M0:

$$\mathbf{RM1} = \mathbf{KM1} \cdot \mathbf{CM1F}$$

$$\mathbf{RM2} = \mathbf{KM2} \cdot (\mathbf{CM1F} + \mathbf{KAKG} \cdot \mathbf{CAKG})$$

The original position is M1:

$$\mathbf{RM1} = \mathbf{KM21} \cdot (\mathbf{CM1F} - \mathbf{KAKG} \cdot \mathbf{CAKG})$$

$$\mathbf{RM2} = \mathbf{KM12} \cdot (\mathbf{CM2F} + \mathbf{KAKG} \cdot \mathbf{CAKG})$$

The original position is M2:

$$\mathbf{RM2} = 1$$

Macrophage migration: MO and MC are the intensity coefficients of the effects of oxygen concentration and chemical attractants on macrophage movement. IL-6 and IL-10 were considered as the chemoattractant in our study.

$$\mathbf{Px} + 1 = (\mathbf{MO} \cdot \Delta\mathbf{Ox} + 1 + \mathbf{MC} \cdot \Delta\mathbf{Chemox} + 1)$$

2.24.4 | Microenvironment scale

The microenvironment scale includes glucose, oxygen, EGF, NO, VEGF, α -KG, IL-6, IL-10 and other cytokines (Supplementary Figure S1A). We used a set of reaction-

diffusion ODEs to show the dynamic evolution of metabolites and cytokines in the microenvironment. Using the change of glucose concentration as an example: G represents the concentration of glucose; Δ is the Laplace operator; D_G is the diffusivity of glucose; $q_G = 2\pi r p_G$, p_G is the vascular permeability of glucose, r is the average radius of blood vessels, G^{blood} is concentration of glucose in the blood, U_G is the glucose uptake rate of the cell. If there are blood vessels, the time-related characteristic function $X_{\text{ves}}(t, x)$ is equal to 1. Otherwise, it is equal to 0. $X_{\text{tum}}(t, x)$ is equal to 1 in the tumor area or 0 in other places. In each simulation step, X_{ves} and X_{tum} are updated according to the development of the tumor and its microvascular distribution. Our model assumes that the vascular transport of glucose, O_2 and trastuzumab as well as NO attenuation are considered. The coefficients are in Supplementary Table S12. The specific equations are as follows:

$$\text{Glucose : } \frac{\partial G}{\partial t} = D_G \Delta G + X_{\text{ves}}(t, x) q_G (G^{\text{blood}} - G) - X_{\text{tum}}(t, x) U_G$$

$$O_2 : \frac{\partial C}{\partial t} = D_C \Delta C + X_{\text{ves}}(t, x) q_C (C^{\text{blood}} - C) - X_{\text{tum}}(t, x) U_C$$

$$\text{EGF : } \frac{\partial E}{\partial t} = D_E \Delta E + X_{M2}(t, x) S_E$$

$$\text{NO : } \frac{\partial N}{\partial t} = D_N \Delta N + X_{M1}(t, x) S_N - O_N N$$

$$\text{VEGF : } \frac{\partial V}{\partial t} = D_V \Delta V + X_{M2}(t, x) S_V + X_{\text{tum}(\text{apo})}(t, x) S_V$$

$$\text{AKG : } \frac{\partial A}{\partial t} = D_{AKG} \Delta AKG + X_{M2}(t, x) S_{AKG} + X_{\text{tum}(\text{act})}(t, x) S_{AKG}$$

2.24.5 | Tissue scale

The sprouting of neovascularization is induced by VEGF secreted by tumor cells and M2 macrophages. Fibronectin comes from endothelial cells, and β and γ represent its production and uptake rates.

$$\text{VEGF : } \frac{\partial V}{\partial t} = D_V \Delta V + X_{M2}(t, x) S_V + X_{\text{tum}(\text{apo})}(t, x) S_V$$

$$\text{Fib} : \frac{\partial \mathbf{F}}{\partial t} = X_{\text{ves}}(t, x)\beta - X_{\text{tum}}(t, x)\gamma \mathbf{F}$$

The apical endothelial cells of neovascularization respond to the chemotaxis of VEGF and fibronectin gradients. The migration probabilities of apical endothelial cells in four directions are as follows (Supplementary Figure SIC).

$$\mathbf{P}_k \propto \left(\alpha \frac{k_v}{k_v + V} V + \gamma \nabla V \right) \cdot \text{lk} \dots \dots k = 1, 2, 3, 4$$

$$\mathbf{P}_1 = \frac{k_1}{(k_1 + V(i, j))} \times (V(i + 1, j) - V(i, j)) + K_2 \\ \times (f(i + 1, j) - f(i, j))$$

$$\mathbf{P}_2 = \frac{k_1}{(k_1 + V(i, j))} \times (V(i - 1, j) - V(i, j)) + K_2 \\ \times (f(i - 1, j) - f(i, j))$$

$$\mathbf{P}_3 = \frac{k_1}{(k_1 + V(i, j))} \times (V(i, j + 1) - V(i, j)) + K_2 \\ \times (f(i, j + 1) - f(i, j))$$

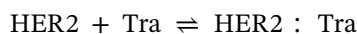
$$\mathbf{P}_4 = \frac{k_1}{(k_1 + V(i, j))} \times (V(i, j - 1) - V(i, j)) + K_2 \\ \times (f(i, j - 1) - f(i, j))$$

2.24.6 | Trastuzumab therapy and combined therapy

Trastuzumab represses downstream molecular pathways by binding with HER2. The equations describing the binding process of HER2 and measuring the residual amount are as follow: $[HER2]_0$ represents the initial concentration of HER2, and k_m is the Michaelis constant.

$$\text{Tra} : \frac{\partial \text{Tra}}{\partial t} = D_{\text{tra}} \Delta \text{Tra} + X_{\text{ves}}(t, x) q_{\text{tra}} (V_{\text{tra}} - V) - X_{\text{tum}}(t, x) U_{\text{tra}}$$

$$[HER2]_{\text{eff}} = [HER2]_0 - [HER2 : \text{Tra}]$$



$$[HER2 : \text{Tra}] = \frac{[HER2]_0 [\text{Tra}]}{k_m + [\text{Tra}]}$$

The final output was obtained by inputting the observation time and the parameters of treatment plan by

MATLAB. The equations of combination treatment were as follows. K_0 indicates the combined effect of anti-angiogenesis drug and vascular endothelial growth factor receptor (VEGFR); D_0 indicates the effect of reversing macrophage polarization; $Sakg1$ and $Sakg2$ represent α -KG generation rate from tumor cells and M2 macrophages after the use of GLS inhibitors (Supplementary Figure SID). The coefficients are listed in Supplementary Table S13.

$$\text{Efficacy of anti-angiogenesis therapy: } VEGF_{t+1} = K_0 \cdot VEGF_t$$

$$\text{Pro M1 polarization: } KM12_{t+1} = D_0 \cdot KM12_t$$

$$\text{GLS inhibitors: } \Delta AKG_t = 1_{\text{tum}} \cdot SAKG1 + 1_{M2} \cdot SAKG2$$

The above combination drugs were used to simulate the efficacy of drugs based on biomedical studies, regardless of the pharmacokinetics of individual heterogeneity and dose studies in clinical trials.

2.25 | Efficacy assay of combined treatment in mouse model

To evaluate the efficacy of different combination therapies, 1×10^6 NCI-N87-TR cells were injected into the right flank of nude mice. Tumor measurement and grouping method were performed as previously described at 2.11. The mice were randomly divided into seven experimental groups (6-8 mice for each group): PBS; trastuzumab; trastuzumab + BPTES; trastuzumab + BPTES + celecoxib; trastuzumab + BPTES + B20-4.1.1; trastuzumab + B20-4.1.1 + celecoxib; trastuzumab + BPTES + celecoxib + B20-4.1.1. The following 3-week treatments were given as one or as a combination of the following: PBS, trastuzumab and BPTES are the same with 2.11; celecoxib (HY-14398, MedChemExpress, Princeton, NJ, USA), 80 mg/kg, intragastrical administration, every other day; B20-4.1.1 (Genentech, South San Francisco, CA, USA), 5 mg/kg, intraperitoneal injection, twice a week. Tumor volumes and weights were measured and recorded, and the mice were euthanized by cervical dislocation at the end of treatment.

2.26 | Statistical analysis

The quantitative data were presented as mean \pm standard deviation (SD). SPSS 22.0 software (IBM SPSS, Chicago, IL, USA) was used for statistical analysis. Differences between experimental groups were assessed using Student's *t*-test or one-way analysis of variance. Survival

analysis of tumor-bearing mice was performed using the Kaplan-Meier method and compared by the log-rank test. Differences were considered statistically significant if P values < 0.05 .

3 | RESULTS

3.1 | Glutamine metabolism was increased in trastuzumab-resistant HER2-positive gastric cancer

To explore the relationship between trastuzumab resistance and metabolic reprogramming, RNA-seq of the trastuzumab-sensitive and trastuzumab-resistant cell lines was performed. Metabolic pathway scores in the KEGG database were calculated using the GSVA method. The heat map showed that multiple metabolic pathways were enhanced in trastuzumab-resistant cells, such as glucose and lipid metabolism (Figure 1A), consistent with previous reports [13–15]. Specifically, the glutamine metabolic pathway score was significantly upregulated (Figure 1B), suggesting that glutamine metabolism may be involved in trastuzumab resistance.

To verify the results of the cell experiments, we collected HER2-positive gastric cancer tissues from trastuzumab-sensitive and trastuzumab-resistant patients for transcriptome sequencing and found that amino acid metabolism scores increased in trastuzumab-resistant patients by GSVA scoring of the KEGG metabolic pathway (Supplementary Figure S2A). Further analysis of the amino acid metabolism showed that the glutamine metabolic pathway score was significantly upregulated in the trastuzumab-resistant group (Supplementary Figure S2B–C). Differential gene enrichment analysis also revealed that trastuzumab-resistant patients were significantly enriched in glutamine metabolic pathways (Supplementary Figure S2D). The above suggests that the sequencing results of tumor tissue were consistent with the results of increased glutamine metabolism in trastuzumab-resistant cells.

To further validate the role of glutamine metabolism in trastuzumab resistance, glutamine metabolism-related genes were detected by qRT-PCR in trastuzumab-sensitive and trastuzumab-resistant cells. The results showed that glutamine metabolism-related indicators were increased in trastuzumab-resistant cells, with the most significant increase in GLS1 (Figure 1C). WB also showed that GLS1 expression was increased in trastuzumab-resistant cells (Figure 1D). In addition, NCI-N87 and NCI-N87-TR cells were subcutaneously injected into nude mice. IF staining revealed higher GLS1 expression in trastuzumab-resistant

tissue than in trastuzumab-sensitive tissue (Figure 1E). The activity of glutaminase and the levels of the metabolic products α -KG and glutamate were also significantly increased in trastuzumab-resistant cells (Figure 1F) and tumor tissue of nude mice (Figure 1G). In conclusion, we confirmed that glutamine metabolism was increased in trastuzumab-resistant cells both in vitro and in vivo.

To investigate the relationship between elevated glutamine metabolism and trastuzumab resistance, the GLS1 inhibitors BPTES and CB839 were used for interference experiments. The MTT assay showed that trastuzumab or GLS1 inhibitors did not significantly change the proliferation of trastuzumab-resistant cells, whereas BPTES or CB839 combined with trastuzumab partially inhibited the proliferation of trastuzumab-resistant cells (Figure 1H). Furthermore, through flow cytometry, we also found that the apoptosis rate was increased in trastuzumab-resistant cells treated with trastuzumab in combination with either BPTES or CB839, but not as much as that in the trastuzumab-sensitive cells treated with trastuzumab alone (Figure 1I). In addition, we designed GLS1-silenced trastuzumab-resistant cells, with GLS1 silencing effect validated by WB and qRT-PCR (Supplementary Figure S2E–F). The sensitivity of shGLS1 trastuzumab-resistant cells to trastuzumab was detected by MTT and flow cytometry to further investigate the role of GLS1 in trastuzumab resistance (Supplementary Figure S2G–H). Similarly, GLS1 silencing partially restored trastuzumab sensitivity. Taken together, we found that inhibition of GLS1 function and expression partially increased trastuzumab sensitivity of trastuzumab-resistant cells.

Furthermore, we tested the effects of the GLS1 inhibitors in vivo. NCI-N87 and NCI-N87-TR subcutaneous tumor-bearing nude mice were treated with PBS, trastuzumab, BPTES, or BPTES combined with trastuzumab (Figure 1J). The weight and volume statistics of subcutaneous tumors in mice suggested that the trastuzumab-sensitive tumors were significantly suppressed after trastuzumab treatment, while the tumor volume of the trastuzumab-resistant group treated with trastuzumab or BPTES alone did not significantly change compared with trastuzumab-sensitive group. Interestingly, BPTES combined with trastuzumab reduced the tumor size compared to the trastuzumab-resistant group treated with trastuzumab alone, similar to trastuzumab-sensitive group treated with trastuzumab (Figure 1K–L). H&E staining of the heart, liver, spleen, lung, and kidney of the mice did not show organ damage in any group, suggesting limited toxicity (Supplementary Figure S2I). In conclusion, we found that the combination of the glutamine inhibitor BPTES could better reverse trastuzumab resistance in vivo than in cell experiments.

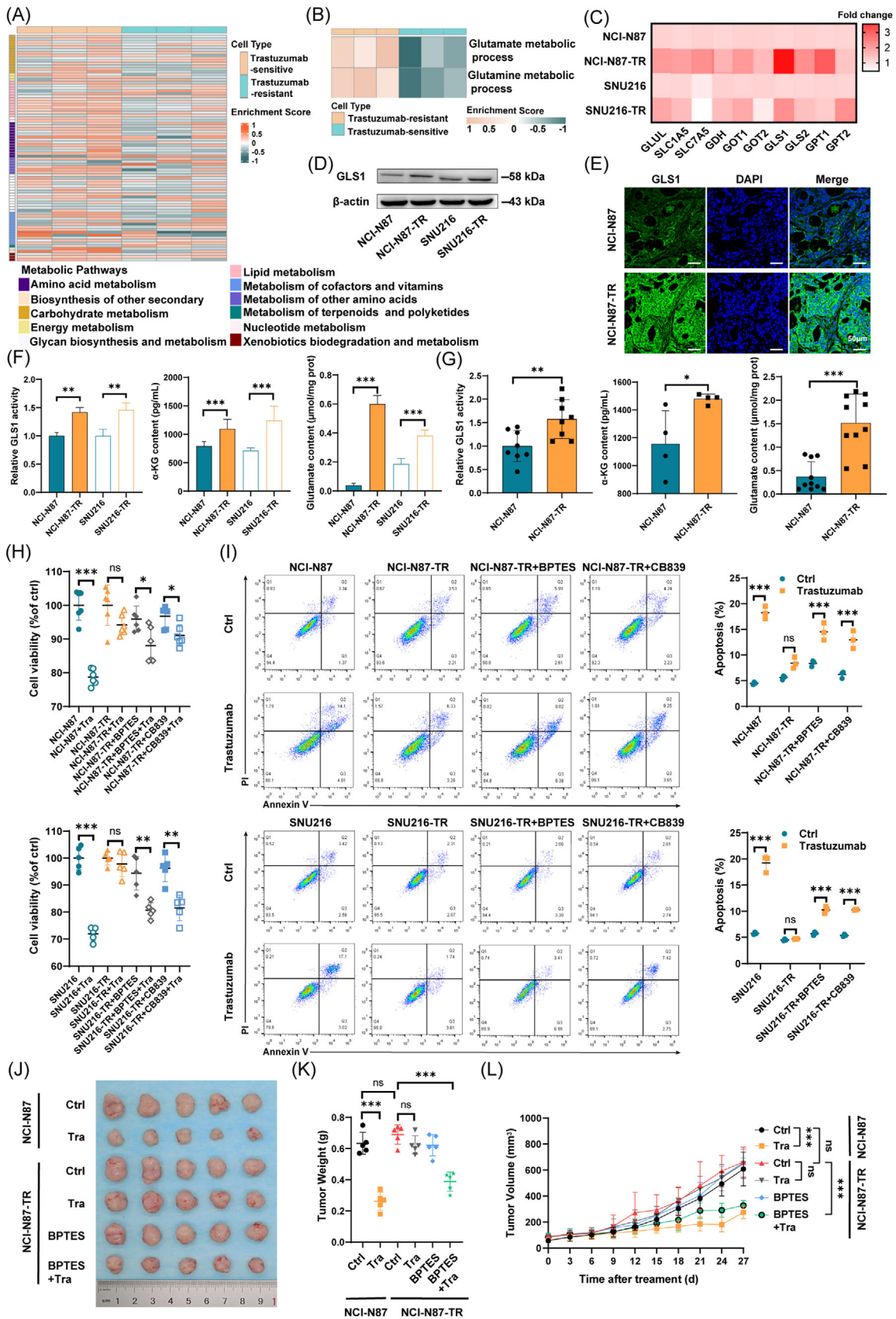


FIGURE 1 Glutamine metabolism was increased in trastuzumab-resistant HER2-positive gastric cancer. (A) GSEA score based on classical 11 metabolic pathways in KEGG database in SNU216 and SNU216-TR cells transcriptome sequencing result. (B) The result of glutamine metabolic score in SNU216 and SNU216-TR cells. (C) Qrt-PCR detection of glutamine metabolism related indexes in NCI-N87,

3.2 | Glutamine metabolism-related M2 macrophage polarization was involved in trastuzumab resistance

Considering the better inhibitory effect of glutamine inhibitors *in vivo*, we speculated there were other cells with high expression of GLS1 in the trastuzumab-resistant microenvironment. First, IHC analysis of GLS1, F4/80, Ly6G, CD31, and α SMA in serial sections of subcutaneous tumors was performed. Interestingly, GLS1 was highly expressed in F4/80-labeled macrophages, but not in other cells in trastuzumab-resistant tumor tissue (Figure 2A). Moreover, IF staining showed that F4/80-labeled macrophages were with high expression of GLS1 (Figure 2B). Finally, macrophages in the tumor tissue were isolated by flow cytometry. The glutaminase activity and glutamate levels of macrophages in the trastuzumab-resistant group were significantly increased (Figure 2C). These results indicated that macrophages exhibited high GLS1 expression and high glutamine metabolism activity in the trastuzumab-resistant microenvironment.

Next, we examined phenotypic changes in the macrophages present in the tumor microenvironment. We used the CIBERSORT tool to analyze the proportion of infiltrating immune cells by RNA-seq in trastuzumab-sensitive and trastuzumab-resistant patients. We found that the proportion of M2 macrophages in trastuzumab-resistant patients was significantly increased, although the proportion of M1 macrophages was decreased insignificantly (Figure 2D). Flow cytometry and IF staining indicated the predomination of CD206-labeled M2 macrophages in the trastuzumab-resistant tumor of mice (Figure 2E-F). Furthermore, we found that CD206-labeled M2 macrophages were significantly

enriched in trastuzumab-resistant tumor tissue from patients (Figure 2G). Taken together, we found that trastuzumab-resistant tumor tissue was highly enriched in GLS1-expressing M2 macrophages.

GLS1 was highly expressed in both tumor cells and macrophages in trastuzumab-resistant tumor tissue. Therefore, we speculated that there is crosstalk in glutamine metabolism between tumor cells and macrophages. To explore the regulatory relationship between the two, we constructed GLS1-silenced trastuzumab-resistant tumor cells and THP-1 macrophages, and then co-cultured them with untreated THP-1 macrophages or trastuzumab-resistant tumor cells, separately. Co-culture assays showed that incubation with GLS1-silenced trastuzumab-resistant tumor cells could significantly decrease GLS1 expression in THP-1 macrophages (Figure 3A-B), indicating that GLS1 may constitute the bridge between trastuzumab-resistant tumor cells and macrophages. However, when co-cultured trastuzumab-resistant tumor cells with GLS1-silenced THP-1 macrophages, no significant change in GLS1 expression was found in tumor cells (Supplementary Figure S3A-B). Therefore, we speculated that tumor cells regulate the expression of GLS1 in macrophages.

We explored the effect of tumor cells on macrophages metabolism and phenotype using co-culture system. After co-culturing with tumor cells, GLS1 expression in macrophages in the trastuzumab-resistant group was significantly increased (Figure 3C-D). Compared with trastuzumab-sensitive cells, GLS1 enzyme activity, α -KG, and glutamate levels in trastuzumab-resistant cells were significantly increased (Figure 3E). In terms of macrophage phenotype, we detected M1 and M2 markers of macrophages by qRT-PCR and found that M1

NCI-N87-TR, SNU216 and SNU216-TR cells. (D) WB analysis of GLS1 protein in NCI-N87, NCI-N87-TR, SNU216 and SNU216-TR cells. (E) Representative IF images of GLS1 (green) and DAPI (blue) in sections of subcutaneous tumors of xenograft nude mice. (F) GLS1 enzyme activity, α -KG content and glutamine content of NCI-N87, NCI-N87-TR, SNU216 and SNU216-TR cells. (G) GLS1 enzyme activity, α -KG content and glutamine content of subcutaneous tumors of xenograft nude mice. (H) MTT assays were performed to investigate the proliferation of NCI-N87, NCI-N87-TR, SNU216 and SNU216-TR cells treated with or without trastuzumab (10 μ g/mL, 48 h), BPTES (20 μ mol/L, 48 h), and CB839 (20 μ mol/L, 48 h). (I) Apoptosis ratios of NCI-N87, NCI-N87-TR, SNU216 and SNU216-TR cells after relative treatment were detected by flow cytometry. Representative images and a histogram of the data are shown. Three independent experiments were performed. (J-L) NCI-N87 and NCI-N87-TR cells were injected into nude mice ($n = 5$). After 7 days, the nude mice started to accept following treatments: trastuzumab (10 mg/kg, twice a week), BPTES (12.5 mg/kg, twice a week). (J) Image of the harvested xenograft tumors; Tumor weight (K) was represented as the means of tumor weight \pm SD; Tumor volume (L) was measured every 3 days until day 27. All of the relative gene expression data were detected by qRT-PCR and normalized to β -actin. The fold changes were relative to those of the control Group. The data are presented as the mean \pm SD. * $P < 0.05$, ** $P < 0.01$, *** $P < 0.001$; ns, nonsignificant.

Abbreviations: HER2, human epidermal growth factor receptor 2; GSEA, gene set variation analysis; KEGG, Kyoto Encyclopedia of Genes and Genomes; TR, trastuzumab-resistant; qRT-PCR, quantitative real-time polymerase chain reaction; α -KG, α -ketoglutarate; GLUL, glutamine synthetase; SLC1A5, solute carrier family 1 member 5; SLC7A5, solute carrier family 7 member 5; GDH, glutamate dehydrogenase; GOT1, glutamic-oxaloacetic transaminase 1; GOT2, glutamic-oxaloacetic transaminase 2; GLS1, glutaminase-1; GLS2, glutaminase-2; GPT1, glutamic-pyruvic transaminase-1; GPT2, glutamic-pyruvic transaminase-2; IF, immunofluorescence; IHC, immunohistochemistry; MTT, 3-[4,5-Dimethylthiazol-2-yl]-2,5-diphenyltetrazolium bromide; Tra, trastuzumab; SD, standard deviation.

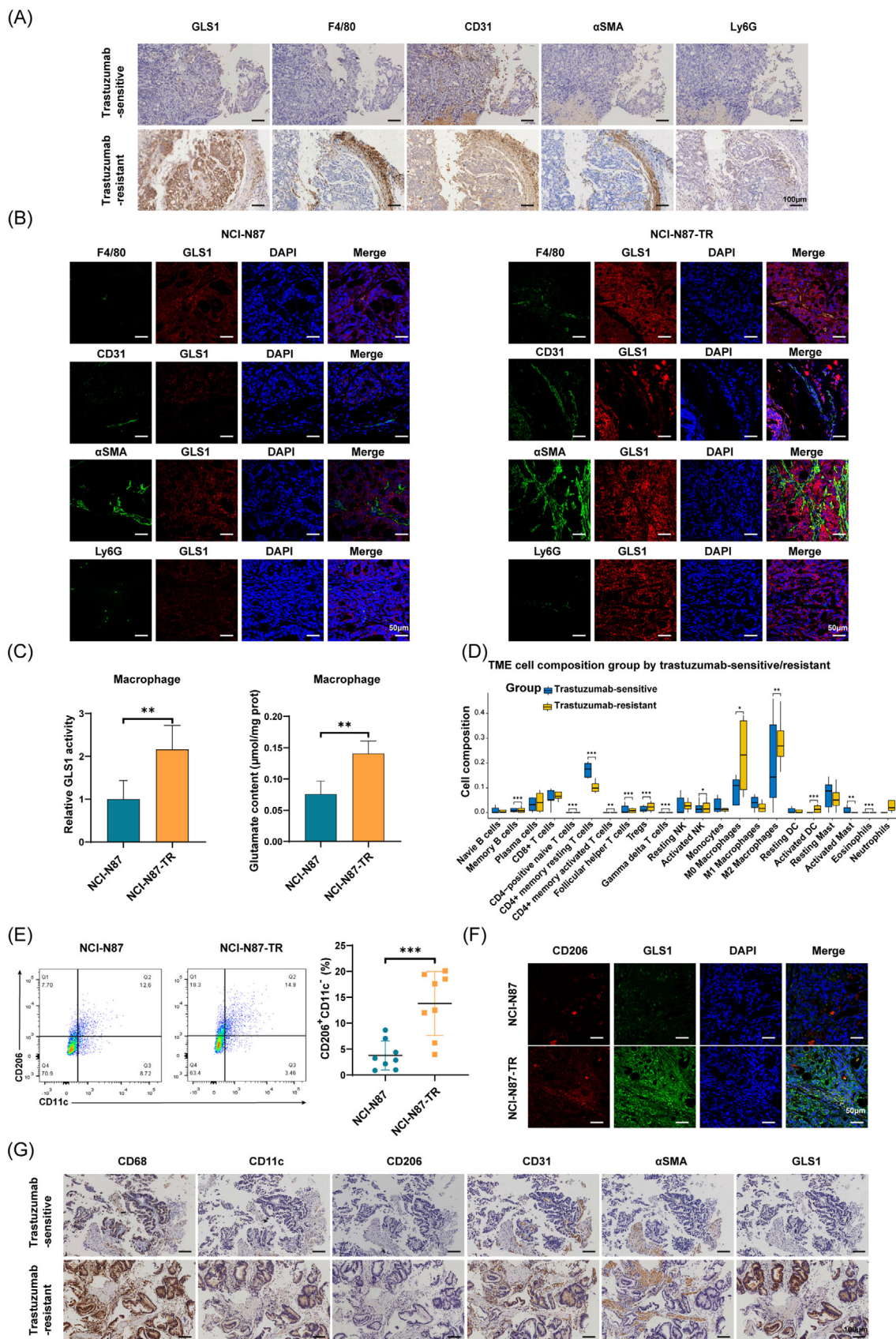


FIGURE 2 Glutamine metabolism-related M2 macrophage polarization was involved in trastuzumab resistance. (A) Representative IHC images of GLS1, F4/80, CD31, α SMA and Ly6G performed on serial sections of subcutaneous tumors of xenograft nude mice. (B) Representative IF images of F4/80, CD31, α SMA, Ly6G (green), GLS1 (red) and DAPI (blue) performed on sections of subcutaneous tumors of

macrophage markers nitric oxide synthase 2 (NOS2), tumor necrosis factor alpha (TNF- α), IL-6, IL-12 were significantly reduced in the trastuzumab-resistant co-culture group, while the expression of M2 markers Arginase 1 (ARG1), CD163, CD206, IL-10, transforming growth factor beta 1 (TGF β 1), and C-C motif chemokine ligand 22 (CCL22) were increased (Figure 3F and Supplementary Figure S3C). Flow cytometry results showed that co-culturing with trastuzumab-resistant cells increased the proportion of M2 macrophages (Figure 3G and Supplementary Figure S3D).

Previous studies have found that macrophages mainly affect tumor growth by affecting T cells or angiogenesis [24, 45]. Based on our study in nude mice, which lacked the effect of T cells, we explored the effect of macrophages on tumor via angiogenesis. First, GSEA revealed that tumor tissue of trastuzumab-resistant patients was significantly enriched in tumor angiogenesis up-regulation pathway (Figure 3H). Second, the supernatant from the co-culture system of tumor cells and macrophages was collected for the chorioallantoic membrane vascular assay. We found a stronger angiogenesis in the trastuzumab-resistant group. Adding IL-4 to the trastuzumab-sensitive group, which acts as an inducer of M2 macrophage polarization, promoted the formation of angiogenesis (Figure 3I). Generally, we suggest that trastuzumab-resistant cells promote angiogenesis through M2 macrophages.

We have identified that trastuzumab-resistant cells induced the M2 phenotype and pro-angiogenesis function of macrophages. Next, we investigated whether tumor cells regulate phenotype and function of macrophages through GLS1. Trastuzumab-resistant cells and macrophages were co-cultured with the GLS1 inhibitors BPTES or CB839 for 48 h. The expression of GLS1 in macrophages was significantly reduced (Supplementary Figure S3E). Meanwhile, M1 macrophage markers were upregulated, and M2 markers were decreased in the BPTES or CB839 treatment groups (Supplementary Figure S3F). Flow cytometry showed that M2 macrophages were decreased in BPTES or CB839 treatment groups (Supplementary Figure S3G). Finally, chorioallantoic membrane vascular assay demon-

strated that angiogenesis in the BPTES treatment group was significantly reduced, whereas that in the IL-4 treatment group was increased (Supplementary Figure S3H). Altogether, tumor cells promote trastuzumab resistance by altering the M2 phenotype and pro-angiogenesis function of macrophages via regulation of glutamine metabolism.

3.3 | Tumor cells secreted GLS1 microvesicles to promote glutamine metabolism and M2 phenotype polarization in macrophages

Next, we explored the mechanism by which tumor cells regulate glutamine metabolism and phenotype of macrophages. A conditioned medium from trastuzumab-sensitive and trastuzumab-resistant cells was used to culture macrophages. WB showed that GLS1 expression in macrophages increased in the trastuzumab-resistant group (Figure 4A). GLS1 enzyme activity, α -KG, and glutamate levels were also elevated in macrophages treated with the conditioned medium from trastuzumab-resistant cells (Figure 4B). In addition, we observed a higher proportion of M2 phenotype in macrophages treated with supernatant from trastuzumab-resistant cells (Figure 4C and Supplementary Figure S4A-B). The supernatant of trastuzumab-resistant cells pretreated with GLS1 inhibitors, or silencing of GLS1, was used for culturing macrophages. Results showed that GLS1 expression in macrophages was significantly decreased (Supplementary Figure S4C). The proportion of M2 macrophages was decreased, whereas that of M1 macrophages was increased (Supplementary Figure S4D). In conclusion, we speculate that trastuzumab-resistant cells may secrete GLS1 metabolism-related substances to regulate glutamine metabolism and the M2 phenotype of macrophages.

Studies have shown that tumor cells can secrete extracellular vesicles to act on recipient cells [28, 46], and recent studies have suggested that GLS1 may function in microvesicles secreted from tumor cells [20, 47]. Therefore, we extracted microvesicles from trastuzumab-sensitive

xenograft nude mice. (C) Macrophages in subcutaneous tumors were isolated, and the GLS1 enzyme activity and glutamine content were detected. (D) CIBERSORT analysis of the proportion of immune cells infiltration in patient tissue. (E) Macrophages isolated from subcutaneous tumors were analyzed for F4/80⁺CD206⁺CD11c⁻ M2 macrophages by flow cytometry ($n = 8$ for each group). (F) Representative IF images of CD206 (red), GLS1 (green) and DAPI (blue) in sections of subcutaneous tumors of xenograft nude mice. (G) Representative IHC images of CD68, CD11c, CD206, CD31, α SMA and GLS1 performed on serial sections of tumor tissue from HER2-positive gastric cancer patients. The data are presented as the mean \pm SD. * $P < 0.05$, ** $P < 0.01$, *** $P < 0.001$; ns, nonsignificant.

Abbreviations: TR, trastuzumab-resistant; IHC, immunohistochemistry, IF, immunofluorescence; GLS1, glutaminase-1; F4/80, mouse EGF-like module-containing mucin-like hormone receptor-like 1; CD31, platelet and endothelial cell adhesion molecule 1; α SMA, alpha-smooth muscle actin; Ly6G, lymphocyte antigen 6 complex locus G; IF, immunofluorescence; DAPI, 4',6-diamidino-2-phenylindole; HER2, human epidermal growth factor receptor 2; SD, standard deviation.

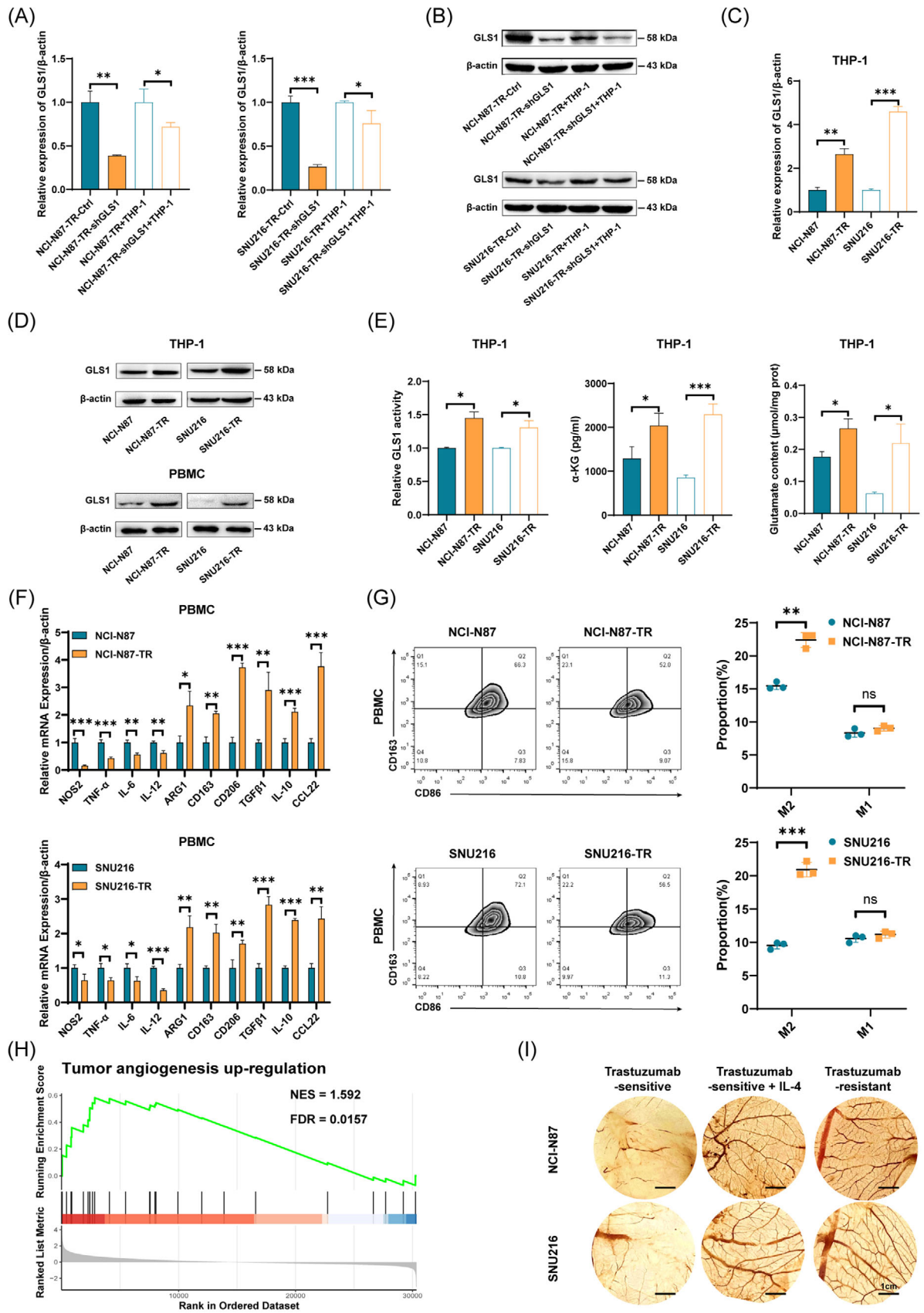


FIGURE 3 Tumor cell regulated GLS1 expression and phenotypic transformation of macrophage. (A) qRT-PCR analysis of mRNA level of GLS1 in trastuzumab-resistant cells transfected with shRNA of GLS1, and in THP-1 co-cultured with trastuzumab-resistant cells transfected with or without shRNA of GLS1. (B) WB analysis of GLS1 protein in trastuzumab-resistant cells transfected with shRNA of GLS1, and in THP-1 co-cultured with trastuzumab-resistant cells transfected with or without shRNA of GLS1. (C) Bar graph showing relative expression of GLS1 in THP-1 cells co-cultured with NCI-N87, NCI-N87-TR, SNU216, and SNU216-TR. (D) Western blot analysis of GLS1 and beta-actin in THP-1 and PBMC cells transfected with NCI-N87, NCI-N87-TR, SNU216, and SNU216-TR. (E) Bar graphs showing relative GLS1 activity, alpha-KG content, and glutamate content in THP-1 cells co-cultured with NCI-N87, NCI-N87-TR, SNU216, and SNU216-TR. (F) Bar graphs showing relative mRNA expression of various cytokines in PBMC cells transfected with NCI-N87 and NCI-N87-TR (top), and SNU216 and SNU216-TR (bottom). (G) Flow cytometry plots and bar graphs showing CD163 and CD86 expression in PBMC cells co-cultured with NCI-N87, NCI-N87-TR, SNU216, and SNU216-TR. (H) GSEA plot showing tumor angiogenesis up-regulation with NES = 1.592 and FDR = 0.0157. (I) Micrographs showing macrophage phenotypic transformation in NCI-N87 and SNU216 cells co-cultured with Trastuzumab-sensitive, Trastuzumab-sensitive + IL-4, and Trastuzumab-resistant cells.

and trastuzumab-resistant cell supernatants by differential centrifugation. TEM and SEM clearly illustrated the structure of extracellular microvesicles and showed that trastuzumab-resistant cells secreted more microvesicles than trastuzumab-sensitive cells (Figure 4D-E). The WB assay was performed subsequently. Compared to whole-cell lysates, microvesicles only expressed the microvesicles markers Flotillin-2, Alix, and transglutaminase 2 (TGM2), but did not express the whole-cell makers $I\kappa B\alpha$ and β -actin. In addition, compared with trastuzumab-sensitive cells, the expression of Flotillin-2, Alix, and TGM2 was significantly upregulated in trastuzumab-resistant cells (Figure 4F). The same results were shown in IF staining (Figure 4G). In conclusion, the above experiments suggest that HER2-positive gastric cancer cells can secrete microvesicles, which are more active in trastuzumab-resistant cells.

Our next goal was to determine whether microvesicles secreted from tumor cells contain the GLS1 protein. First, we detected GLS1 expression in microvesicles by WB, and observed higher GLS1 expression in the microvesicles of trastuzumab-resistant cells (Figure 4F). Second, GLS1 enzyme activity in microvesicles was detected, confirming that GLS1 enzyme activity was significantly higher in trastuzumab-resistant cells than in trastuzumab-sensitive cells (Figure 4H). We further validated this finding at the patient level. IHC staining showed that trastuzumab-resistant tumor tissues expressed more GLS1 and microvesicular indicator TGM2 than trastuzumab-sensitive tumor tissues (Supplementary Figure S4E). In addition, we extracted microvesicles from the blood of patients, and found higher GLS1 enzyme activity in microvesicles from trastuzumab-resistant patients than from trastuzumab-sensitive patients (Supplementary Figure S4F). Taken together, these results suggest that tumor cells secrete GLS1 microvesicles and trastuzumab-

resistant tumor microenvironment contains more GLS1 microvesicles.

Next, we verified that tumor cells regulate macrophage metabolism and phenotype through the secretion of GLS1 microvesicles. Microvesicles of trastuzumab-sensitive and trastuzumab-resistant cells were extracted and then cultured with macrophages. WB assays showed that treatment of microvesicles increased the expression of GLS1 in macrophages, and GLS1 expression in the trastuzumab-resistant group was higher than that in the trastuzumab-sensitive group (Supplementary Figure S4G). Meanwhile, flow cytometry analysis showed that the microvesicles extracted from both trastuzumab-sensitive and trastuzumab-resistant cells could promote M2 polarization of macrophages and that the M2 phenotype in the trastuzumab-resistant group was significantly increased compared with that in trastuzumab-sensitive group (Supplementary Figure S4H). To explore how GLS1 in microvesicles promoted M2 macrophage polarization, we extracted microvesicles to culture macrophages with or without BPTES treatment. Flow cytometry detection showed that the proportion of M2 macrophages was increased in microvesicles group, and decreased in BPTES group, while combined treatment had a reverberating effect (Figure 4I and Supplementary Figure S5A). GLS1 enzyme activity was also detected in these groups (Supplementary Figure S5B). This suggests that trastuzumab-resistant cells secrete more GLS1 microvesicles to promote macrophage GLS1 expression and M2 phenotype.

Next, we used currently recognized extracellular vesicle inhibitor GW4869 to carry out the experiments. We detected vesicle-labeling proteins by IF staining after GW4869 treatment and found that the vesicle-labeling indexes were significantly reduced, suggesting that the inhibitor was effective (Supplementary Figure S5C). We

THP-1 co-cultured with trastuzumab-resistant cells transfected with or without shRNA of GLS1. (C) qRT-PCR analysis of mRNA level of GLS1 in THP-1 co-cultured with NCI-N87, NCI-N87-TR, SNU216 and SNU216-TR cells. (D) WB analysis of GLS1 protein in macrophages co-cultured with NCI-N87, NCI-N87-TR, SNU216 and SNU216-TR cells. (E) GLS1 enzyme activity, α -KG content and glutamine content of THP-1 co-cultured with NCI-N87, NCI-N87-TR, SNU216 and SNU216-TR cells. (F) The M1 phenotype indexes (NOS2, TNF- α , IL-6, IL-12) and M2 phenotype indexes (ARG1, CD163, CD206, TGF β 1, IL-10, CCL22) were confirmed by qRT-PCR in macrophages after co-culturing with NCI-N87, NCI-N87-TR, SNU216 and SNU216-TR cells for 48 h. (G) Flow cytometry detected the expression of CD86 and CD163 in macrophages after co-culturing with NCI-N87, NCI-N87-TR, SNU216 and SNU216-TR cells for 48 h. The proportions of M1 and M2 macrophages were calculated. Bar graphs of the summary data are shown. (H) GSEA analysis showed tumor angiogenesis up-regulation pathway was significantly enriched in the trastuzumab-resistant group. (NES = 1.592, FDR = 0.0157). (I) Chorioallantoic membrane vascular assay detected the angiogenesis after treating with IL-4 (10 ng/mL) or conditioned medium from NCI-N87, NCI-N87-TR, SNU216 and SNU216-TR cells for 48 h. All of the relative gene expression data were detected by qRT-PCR and normalized to β -actin. The fold changes were relative to those of the control Group. The data are presented as the mean \pm SD. * $P < 0.05$, ** $P < 0.01$, *** $P < 0.001$; ns, nonsignificant. Abbreviations: TR, trastuzumab-resistant; GLS1, glutaminase-1; qRT-PCR, quantitative real-time polymerase chain reaction; NOS2, nitric oxide synthase 2; TNF- α , tumor necrosis factor alpha; IL-6, interleukin 6; IL-12, interleukin 12; ARG1, arginase 1; TGF β 1, transforming growth factor beta1; IL-10, interleukin 10; CCL22, C-C motif chemokine ligand 22; α -KG, α -ketoglutarate; GSEA, gene set enrichment Analysis; NES, normalized enrichment score; SD, standard deviation.

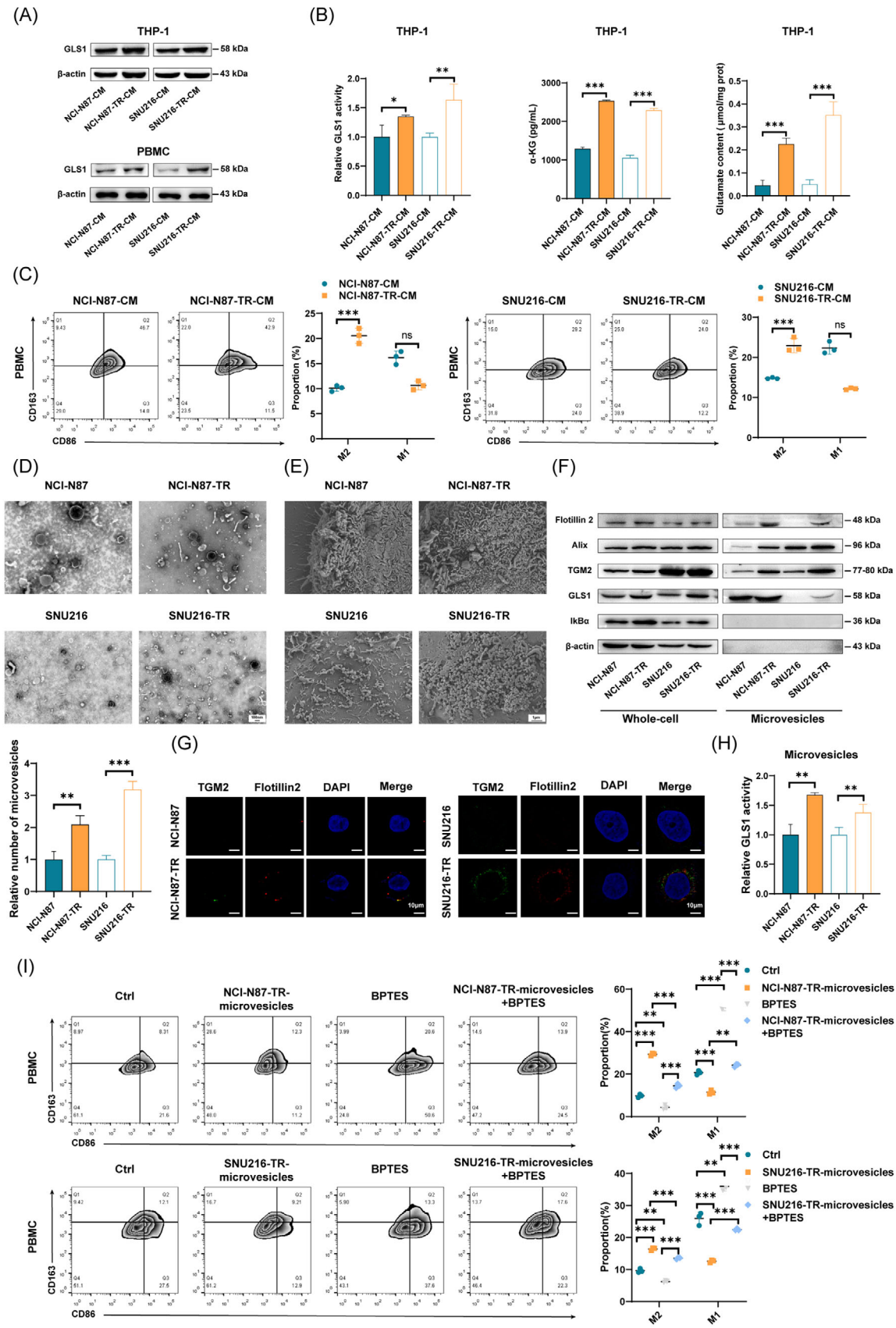


FIGURE 4 Tumor cell promoted the M2 macrophage polarization through GLS1 microvesicle secretion. (A) WB analysis of GLS1 protein in macrophages treated with conditioned medium of NCI-N87, NCI-N87-TR, SNU216 and SNU216-TR cells for 48 h. (B) GLS1 enzyme activity, α-KG content and glutamine content in THP-1 treated with conditioned medium of NCI-N87-TR and SNU216-TR cells for 48 h.

co-cultured macrophages and tumor cells, which were pre-treated with GW4869, and found that GLS1 expression in macrophages was significantly decreased (Supplementary Figure S5D). The proportion of M2 macrophages were also decreased (Supplementary Figure S5E-F). Our experiments confirmed that tumor cells promote glutamine metabolism and phenotypic changes of macrophages by secreting GLS1 microvesicles, and inhibiting microvesicle secretion of tumor cells can reverse GLS1 expression and M2 phenotype polarization of macrophages.

3.4 | CDC42 activated NF- κ B p65 to regulate GLS1 expression and drove GLS1 microvesicle secretion via IQGAP1

Based on the relationship between tumor-derived GLS1 microvesicles and M2 macrophages, we next aimed to delineate the regulatory mechanism for microvesicle secretion. The CDC42 in the Rho GTPase family may be involved in the regulation of GLS1 expression and microvesicle secretion [48]. We found that the expression of CDC42-GTP bound state (GTP-activating CDC42) in trastuzumab-resistant cells was significantly increased (Supplementary Figure S6A). IF staining showed that the expression of microvesicles marker proteins was significantly decreased after the use of ZCL278, a conformation-activating inhibitor of CDC42 (Supplementary Figure S6B). In addition, CDC42 mutant NCI-N87-TR and SNU216-TR cells were constructed with corresponding plasmids: CDC42 wild-type (CDC42-WT), CDC42 G12V mutant (GTPase-activated), and CDC42 T17N mutant (GDPase-locked). The highest GLS1 expression and enzyme activity were found in CDC42 G12V mutant cells with the CDC42 GTP conformation, while inactivated CDC42 T17N mutant cells displayed the lowest level of GLS1 expression and enzyme activity (Figure 5A-B). This suggests that the activation of the CDC42 GTP conformation can promote GLS1 expression. We extracted microvesicles from CDC42 mutant cells and found a similar trend in microvesicles marker

expression and GLS1 enzyme activity in these microvesicles (Figure 5C-D). IF staining analysis of microvesicles markers was consistent with protein detection results (Supplementary Figure S6C). Taken together, these results suggest that the active conformation of CDC42 promotes secretion of GLS1 microvesicles.

Next, we investigated the mechanism by which CDC42 regulated GLS1 expression. Through transcriptome sequencing data analysis, genes positively correlated with GLS1 and CDC42 expression were screened for enrichment analysis and were found to be enriched in the NF- κ B signaling pathway (Figure 5E). The WB assay revealed that the expression of phospho-NF- κ B p65 (Ser536) in trastuzumab-resistant cells was increased (Supplementary Figure S6D). p-NF- κ B p65 expression was also detected in the CDC42 mutants, where the expression was significantly increased in the active conformation and decreased in the inactive conformation (Supplementary Figure S6E). NF- κ B P65 is a transcription factor that activates transcriptional regulation through nuclear translocation [49]. Therefore, we separated and detected the nuclear and cytoplasmic NF- κ B p65 protein expression. The expression of p-NF- κ B p65 in the nucleus and cytoplasm of trastuzumab-resistant cells was significantly increased as detected by WB (Figure 5F). In addition, the subcellular localization of p-NF- κ B p65 in cells was detected by IF staining, and higher expression of p-NF- κ B p65 in the nucleus of trastuzumab-resistant cells was observed (Supplementary Figure S6F). To further clarify whether NF- κ B P65 directly regulates GLS1 by initiating transcription, we conducted a ChIP assay and found that NF- κ B P65 can bind to the promoter region of GLS1 (Figure 5G). We then explored whether CDC42 regulated GLS1 expression in an NF- κ B p65-dependent manner. Trastuzumab-resistant cells were treated with the CDC42 inhibitor ZCL278 and the NF- κ B p65 agonist PMA. WB and GLS1 enzyme activity assays indicated that GLS1 was decreased in the ZCL278 group and increased in the PMA group and that PMA partly reversed the effect of ZCL278 on GLS1 expression and enzyme activity (Figure 5H and Supplementary Figure S6G). These results indicated that

(C) Flow cytometry detected the expression of CD86 and CD163 in macrophages treated with conditioned medium of NCI-N87, NCI-N87-TR, SNU216 and SNU216-TR cells for 48 h. The proportions of M1 and M2 macrophages were calculated. Bar graphs of the summary data are shown. (D) Top, Representative images of negatively stained microvesicles detected by TEM. Bottom, Bar graphs of the summary data are shown. (E) Representative images of microvesicles on cell surfaces taken by SEM. (F) WB analysis of Flotillin 2, Alix, TGM2, GLS1 and I κ B α protein in whole cells and microvesicles isolated from tumor cell supernatant. (G) Representative IF images of TGM2 (green), Flotillin 2 (red) and DAPI (blue) in NCI-N87, NCI-N87-TR, SNU216 and SNU216-TR cells. (H) GLS1 enzyme activity of microvesicles was detected by Kit. (I) Flow cytometry detected the expression of CD86 and CD163 in macrophages treated with or without microvesicles, BPTES (20 μ mol/L) for 48 h. The proportions of M1 and M2 macrophages were calculated. Bar graphs of the summary data are shown. The data are presented as the mean \pm SD. * $P < 0.05$, ** $P < 0.01$, *** $P < 0.001$; ns, nonsignificant.

Abbreviations: TR, trastuzumab-resistant; GLS1, glutaminase-1; α -KG, α -ketoglutarate; TGM2, transglutaminase 2; I κ B α , inhibitor kappa B alpha; IF, immunofluorescence; DAPI, 4',6-diamidino-2-phenylindole; SD, standard deviation.

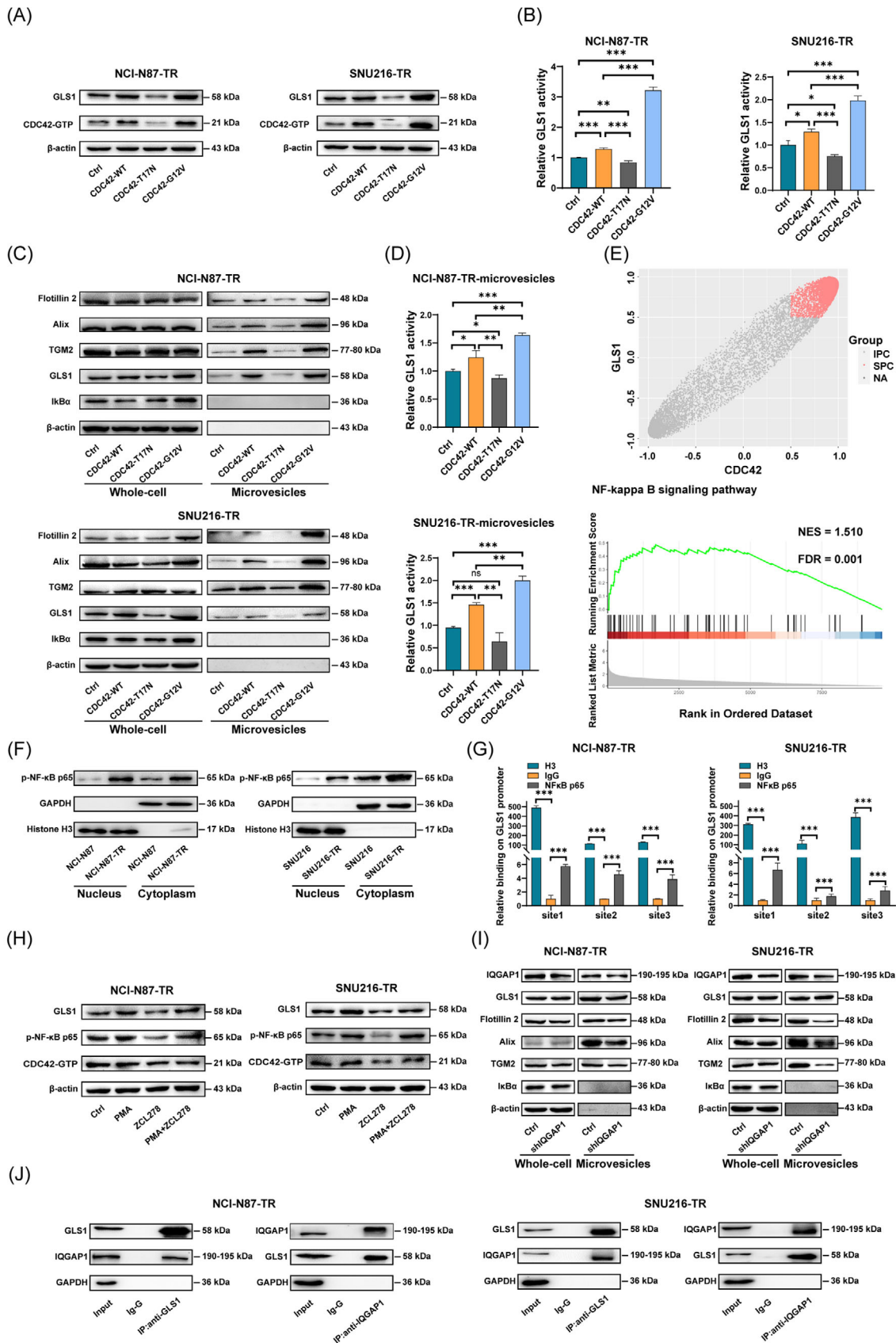


FIGURE 5 CDC42 activated NF-κB p65 to regulate GLS1 expression and drove GLS1 microvesicle secretion via IQGAP1. (A) WB analysis of GLS1 and CDC42-GTP protein in trastuzumab-resistant cells with different CDC42 mutant. (B) GLS1 enzyme activity of trastuzumab-resistant cells with different CDC42 mutant. (C) WB analysis of Flotillin 2, Alix, TGM2, GLS1 and Ixβ protein in

CDC42 promotes GLS1 expression by upregulating the direct transcription factor NF- κ B p65.

To elucidate the mechanism by which CDC42 regulates microvesicle secretion, we analyzed RNA-seq of trastuzumab-sensitive and trastuzumab-resistant cells and found that IQGAP1, a downstream gene of CDC42, was significantly overexpressed in trastuzumab-resistant cells (Supplementary Figure S6H). IQGAP1 has been recognized as the key factor involved in microvesicles formation and secretion [48]. WB assay showed that IQGAP1 expression was increased in trastuzumab-resistant cells (Supplementary Figure S6D). Knocking down IQGAP1 significantly reduced the expression of microvesicles markers (Figure 5I and Supplementary Figure S6I), suggesting that IQGAP1 is involved in microvesicle secretion. Reports have revealed that IQGAP1 acts as a scaffold protein and can regulate its expression by directly binding to other proteins [50, 51]. Through Co-IP assays, we further demonstrated that IQGAP1 could bind to GLS1 (Figure 5J). Therefore, it can be inferred that IQGAP1 can bind to GLS1 and form microvesicles complexes, which participate in the secretion process of GLS1 microvesicles. In conclusion, we confirmed that CDC42-driven GLS1 microvesicle secretion is regulated by downstream IQGAP1-GLS1, together with the activation of NF- κ B p65 to promote GLS1 expression.

3.5 | Establishment of the ABM based on the trastuzumab-resistant microenvironment and selection of treatment strategy

Through combining the dynamic evolution of tumors and microenvironment, we established a mathematical model to simulate the whole dynamic evolution pro-

cess and to explore the best combined treatment strategy in trastuzumab resistance in order to provide a certain reference value for clinical application.

We established a tumor growth model of HER2-positive gastric cancer treated with trastuzumab involving four scales: molecular, cell, microenvironment and tissue (Figure 6A and Supplementary Figure S1A-C). The molecular scale consists of the HER2-EGFR signaling pathway and its downstream cell cycle pathway. The cellular scale mainly includes proliferation, migration and phenotypic transformation of tumor cells and macrophages. The microenvironmental scale involves cytokines and metabolites such as α -KG, EGF, VEGF, NO, IL-6, and IL-10. The tissue scale describes neovascularization and blood vessels that carry nutrients and drugs.

Under natural growth conditions (control group), the number of tumor cells increased significantly when the simulation time was prolonged by 30, 60, 90, and 100 h (Figure 6B). When we used trastuzumab to treat tumor tissues containing trastuzumab-sensitive HER2-positive gastric cancer cells (labeled “TS + Tra”), both angiogenesis and the number of tumor cells decreased significantly compared to those in the control group. There were no differences in tumor tissues containing trastuzumab-resistant HER2-positive gastric cancer cells after trastuzumab treatment (labeled “TR + Tra”) compared with the control group. In addition, the number of active tumor cells also decreased dramatically in the “TS + Tra” group, suggesting a long period of stagnant growth. However, no significant changes in active tumor cells were observed in the “TR + Tra” group (Figure 6B-C). As for the phenotype and number of macrophages in the microenvironment, the number of M2 macrophages in the three models increased gradually with tumor progression, while M1 macrophages displayed a sharp decrease in the “TR + Tra” group

trastuzumab-resistant cells with different CDC42 mutant and microvesicles isolated from those cell's supernatant. (D) GLS1 enzyme activity of microvesicles isolated from trastuzumab-resistant cells with different CDC42 mutant. (E) Top, genes significantly positively correlated with CDC42 and GLS1 were analyzed; Bottom, the differential genes between trastuzumab-sensitive cells and trastuzumab-resistant cells, which positively correlated with CDC42 and GLS1, were enriched into NF- κ B pathway (NES = 1.510, FDR = 0.001). (F) WB analysis of p-NF- κ B p65 protein in nucleus and cytoplasm of trastuzumab-sensitive and trastuzumab-resistant cells. (G) Trastuzumab-resistant cells were harvested for ChIP assay to detect the enrichment of NF- κ B p65 around the GLS1 promoter. Immunoprecipitated DNA was analyzed by qRT-PCR with specific primers. Anti-H3 antibody was used as the positive control. Anti-IgG antibody was used as the negative control ($n = 3$). (H) WB analysis of GLS1, p-NF- κ B p65 and CDC42-GTP protein in trastuzumab-resistant cells treated with or without NF- κ B agonist PMA (50 nmol/L, 48h) and CDC42-GTP inhibitor ZCL278 (10 μ mol/L, 48h). (I) WB analysis of IQGAP1, GLS1, Flotillin 2, Alix, TGM2 and I κ B α protein in trastuzumab-resistant cells transfected with control plasmid or siRNA of IQGAP1 and microvesicles isolated from those cell's supernatant. (J) Co-IP assay was used to detect the protein-protein binding of IQGAP1 and GLS1. Left, GLS1 antibody coprecipitating IQGAP1. Right, IQGAP1 antibody coprecipitating GLS1. Input, protein expression in cell lysates. IgG, negative control. IP, expression of compound coprecipitated by GLS1 or IQGAP1 antibody. The data are presented as the mean \pm SD. * $P < 0.05$, ** $P < 0.01$, *** $P < 0.001$; ns, nonsignificant.

Abbreviations: TR, trastuzumab-resistant; GSEA, gene set enrichment analysis; NES, normalized enrichment score; CDC42, cell division cycle 42; GLS1, glutaminase-1; NF- κ B, nuclear factor kappa B; IQGAP1, IQ motif containing GTPase activating protein 1; TGM2, transglutaminase 2; I κ B α , inhibitor kappa B alpha; ChIP, Chromatin Immunoprecipitation; PMA, phorbol 12-myristate 13-acetate; Co-IP, co-immunoprecipitation; SD, standard deviation.

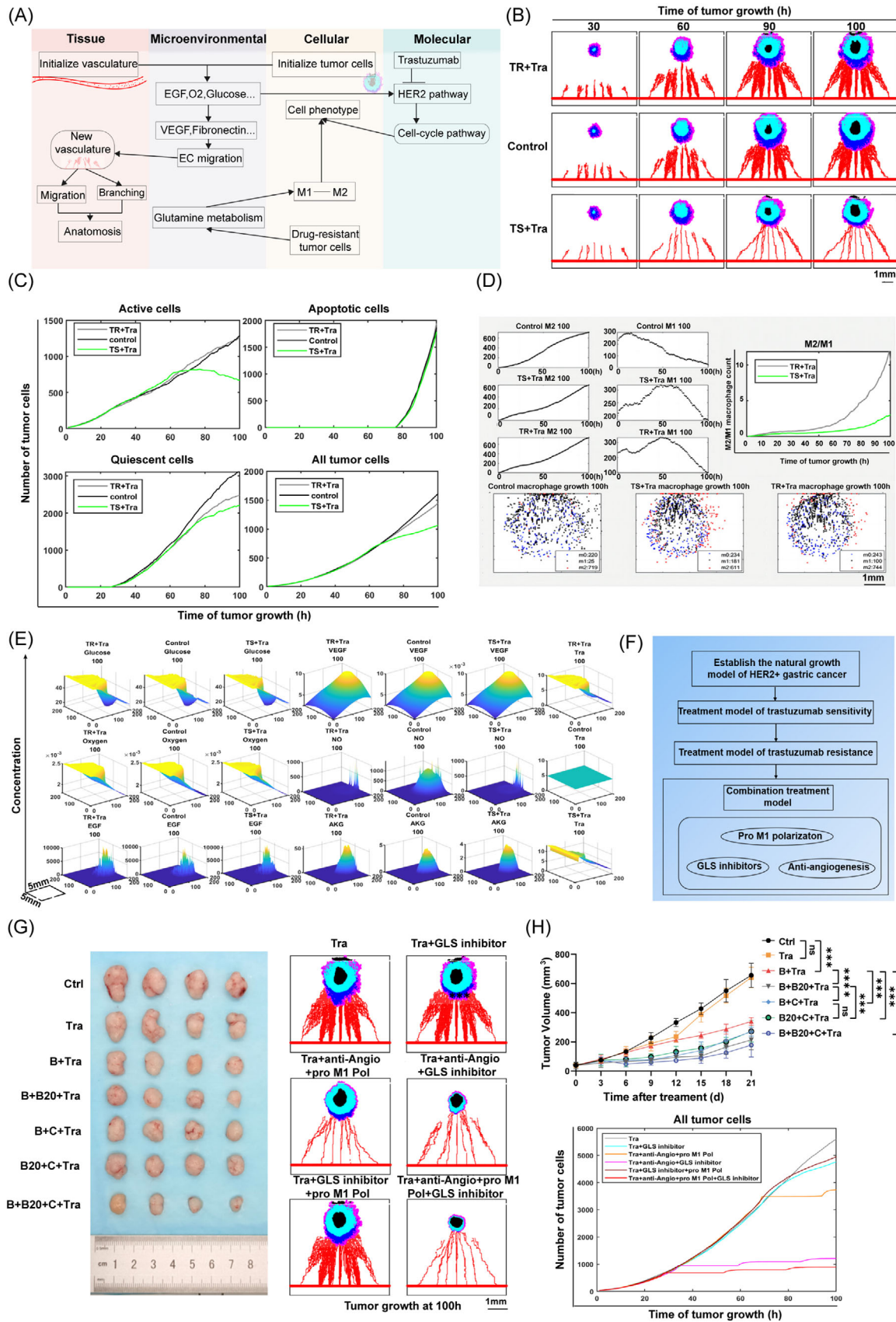


FIGURE 6 Establishment of the ABM based on trastuzumab resistance microenvironment and selection of treatment strategy. (A) The ABM consists of molecular scale, cellular scale, microenvironment scale and tissue scale. Blood vessels transport nutrients, cytokines and metabolites, while VEGF and fibronectin influence vascular growth and migration. Trastuzumab and cytokines affect tumor cell proliferation

(Figure 6D). The visualization and quantification of key cytokines and metabolic components in the three models are shown (Figure 6E). These results are consistent with the results of the animal experiments, which proves the success of our mathematical model construction.

The trastuzumab resistance model revealed that the trastuzumab-resistant microenvironment presented a state of high glutamine metabolism, high M2 macrophage population, and high angiogenesis. Therefore, we developed three corresponding treatment strategies: using anti-angiogenesis drugs (B20-4.1.1), anti-glutamine metabolism inhibitors (BPTES) and pro-M1 polarization therapy (celecoxib) (Figure 6F and Supplementary Figure S1D). We next validated five monotherapy and combination treatment strategies to reverse trastuzumab resistance, including BPTES, BPTES + B20-4.1.1, BPTES + celecoxib, B20-4.1.1 + celecoxib and BPTES + B20-4.1.1 + celecoxib. Among the five therapeutic strategies, we found that the efficacy of BPTES monotherapy in reversing trastuzumab resistance was limited, which was consistent with the result of cellular experiments. Combination treatment of BPTES + B20-4.1.1 had the best efficacy among the three two-drug treatment strategies. However, the three-drug combination treatment had the most significant effect in reversing trastuzumab resistance compared to all other treatment strategies. Similar results were obtained in the animal experiments (Figure 6G-H).

4 | DISCUSSION

In this study, we found that increased glutamine metabolism promotes trastuzumab resistance in HER2-

positive gastric cancer, which promoted M2 macrophage polarization and angiogenesis through GLS1 microvesicles. Mathematical and animal models have been used to identify effective combination strategies to reverse trastuzumab resistance (Figure 7). Transcriptional sequencing and metabolomic analysis of trastuzumab-sensitive and trastuzumab-resistant cell lines and patient tumor tissue revealed that glutamine metabolism in amino acid metabolism was significantly upregulated in trastuzumab-resistant group. Currently, research on the mechanism of trastuzumab resistance in HER2-positive gastric cancer is mainly focused on glucose metabolism and fatty acid metabolism. Previous studies have shown that glycolysis and cholesterol metabolism are upregulated in trastuzumab-resistant cells, and targeted metabolism can increase trastuzumab sensitivity [14, 15]. Our experiments showed that increased glutamine metabolism is associated with trastuzumab resistance, and targeting glutamine metabolism can reverse trastuzumab resistance in vitro and in vivo.

Our study found that all glutamine catabolism-related transporters and metabolic enzymes were increased in trastuzumab-resistant cells, with the expression of GLS1 being the most significant. Previous studies have found that glutamine catabolism depends on mitochondrial glutaminase activity and that the conversion of glutamine to glutamate is involved in biosynthesis and energy metabolism [14, 15]. Glutaminase includes kidney-type (GLS1) and liver-type (GLS2) isoenzymes, and GLS1 is the main research topic. Analysis based on The Cancer Genome Atlas data showed that GLS1 is highly expressed in various malignant tumors, such as gastric cancer, colorectal cancer, breast cancer, glioma, lung

and phenotypic transition by affecting HER2 downstream signaling pathway. Tumor cells affect macrophage polarization through metabolites. (B) 2D Visualization of tumor cell phenotype and size of different models including Control, "TS + Tra" and "TR + Tra" at 30, 60, 90, and 100 h. The red curves represent the growth and migration of new blood vessels, and the red line at the bottom represents the original blood vessels. In the tumor area, black represents necrotic region, light blue represents quiescent region, dark blue represents activated region, and pink represents migratory region. The larger area of activation region is, the larger the tumor size will be in the future, implying the growth potential of the tumor. (C) Growth curves of different regions of the tumor shown in Figure 6B for 100 h. (D) Visualized distribution, number and ratio of M2 and M1 macrophages simulated for 100 h. The data at the lower right corner show the number of monocytes, M1 and M2 macrophages in different groups at 100 hours of tumor growth with the same initial cell number. (E) Visualization of concentration and distribution of key metabolites and cytokines at 100 h. The horizontal plane represents the two-dimensional distribution plane of each substance, and the vertical axis represents the magnitude of the concentration. The unit of concentration for each substance is the same as the unit of concentration in Supplementary Table S5. (F) Schematic diagram of mathematical model construction and application steps. (G) Visualization and quantification of tumor size based on mathematical modeling of trastuzumab resistance to simulate combination therapy strategies. The results of animal experiments (Left), and the results of mathematical modeling (Right) are shown. (H) Top, broken line graphs of tumor volume over time in vivo experimental. Bottom, tumor number over time in the mathematical model under different combination treatment strategies. The data are presented as the mean \pm SD. * $P < 0.05$, ** $P < 0.01$, *** $P < 0.001$; ns, nonsignificant. Notes: Control, untreated and naturally occurring tumors; TS + Tra, trastuzumab-sensitive tumors treated with trastuzumab; TR + Tra, trastuzumab-resistant tumors treated with trastuzumab; anti-Angio, angiogenesis inhibitors; pro M1 Pol, M1-promoting polarimetric drugs. Abbreviations: ABM, agent-based model; EGF, epidermal growth factor; VEGF, vascular endothelial growth factor; HER2, human epidermal growth factor receptor 2; Tra, trastuzumab; AKG, α -Ketoglutarate; B, BPTES; B20, B20-4.1.1; C, Celecoxib.

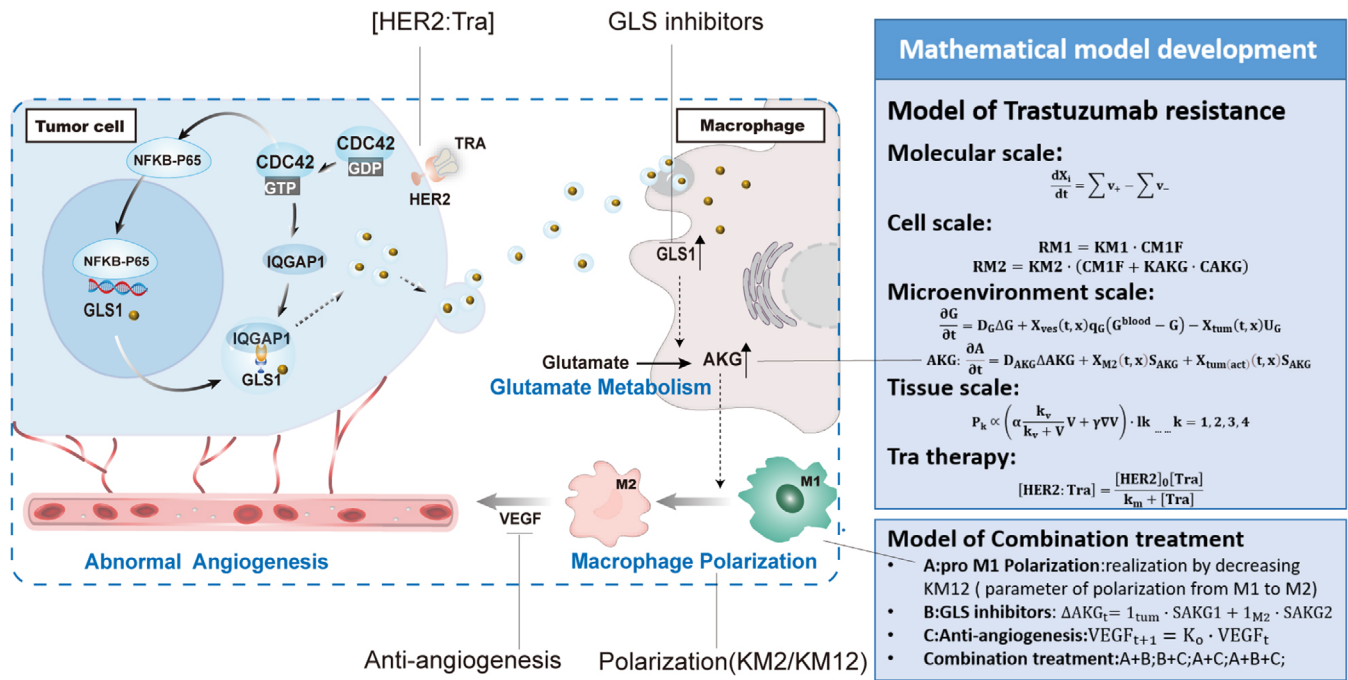


FIGURE 7 Schematic illustration. The mechanism of tumor cells derived GLS1 microvesicles contribute to trastuzumab resistance by promoting M2 macrophage polarization and tumor angiogenesis.

adenocarcinoma, and melanoma, and is associated with poor prognosis [20, 52]. A study on breast cancer have found that HER2 could regulate the expression of GLS1 [53]. Additionally, multiple studies have found that the expression of GLS1 is associated with treatment resistance [20, 52]. In breast cancer, the expression of the GLS1 was found to increase in paclitaxel-resistant cells, and inhibition of GLS1 could reverse the sensitivity of paclitaxel [54]. A study on colorectal cancer found that GLS1 expression promotes oxaliplatin resistance [55]. However, there has been no research on regulating of GLS1 expression and treatment resistance in gastric cancer. Our study found that the expression of GLS1 is increased in trastuzumab-resistant cells, which promotes glutamine metabolism and leads to trastuzumab resistance.

We found that GLS1 inhibitors partially reversed trastuzumab resistance in vitro, whereas they had limited efficacy in reversing trastuzumab resistance in mouse subcutaneous tumors. In the past, the glutaminase inhibitor JHU083 was found to inhibit tumor growth by enhancing the proliferation and activation of CD8 + T cells in various tumors, such as colon cancer, lymphoma, and melanoma [56]. In addition, in a triple-negative breast cancer immunotherapy-resistant model, using glutamine metabolism inhibitors inhibited myeloid-derived suppressor cell (MDSC) infiltration, tumor-associated macrophage (TAM) reprogramming, and immunogenic tumor cell death [57]. Therefore, we detected GLS1 expression in tumor microenvironment and found that F4/80 positive

macrophages highly expressed GLS1, with the M2 phenotype being the dominant phenotype. Previous studies have shown that M2 macrophages are associated with an immunosuppressive microenvironment and promote tumor proliferation and progression by secreting factors that regulate T cells and angiogenesis [24, 45, 58]. No study has explored the relationship between trastuzumab resistance and the macrophage phenotype. In HER2-positive breast cancer, MDSC, macrophages and neutral particles were detected, and only F4/80-labeled macrophages were significantly activated after trastuzumab treatment, dominated by M1 macrophages [59]. Additionally, a previous study found that targeting CD47, an immune checkpoint of macrophage, can reverse trastuzumab resistance [60]. Thus, trastuzumab resistance is closely associated with macrophage. Our study also showed that the resistant microenvironment enriched M2 macrophages with high GLS1 expression, leading to trastuzumab resistance by promoting angiogenesis.

There was a strong metabolic interaction between tumor cells and macrophages. On the one hand, tumor cells regulate the function and phenotype of macrophages by secreting metabolites, metabolic enzymes and extracellular vesicles. Similarly, macrophages can regulate malignant biological phenotypes of tumor cells, such as proliferation and invasion by secreting soluble factors [23, 24, 61]. Previous studies have shown that extracellular vesicles mediate signaling between microenvironment components, and between tumor cells and macrophages [24, 26]. However,

metabolic enzyme microvesicles transfer has only been reported between cancer-associated fibroblasts and tumor cells [24]. Our study found that tumor cells secrete GLS1 microvesicles, which mediates metabolic transmission between tumor cells and macrophages. Studies on GLS1 microvesicles have focused on macrophages and microglia in the nervous system during infection [29, 62]. We proved the existence of GLS1 microvesicles in HER2-positive gastric cancer cells by WB and enzyme activity experiments. Meanwhile, the cell experiments proved that GLS1 microvesicles had enzyme activity, which could promote GLS1 expression and enzyme activity of recipient macrophage, as well as the phenotype of macrophage. Therefore, our results indicate that tumor cells can secrete microvesicles containing metabolic enzymes, which can directly activate downstream intracellular metabolic pathways and change cell phenotypes.

Recent studies on breast and cervical cancer suggest that Ras homolog family member A (RhoA), Rac, and CDC42 of the Rho-GTPase family may be involved in microvesicles formation as key regulators of actin [28, 63]. In a 2021 breast cancer study, Wang et al. identified CDC42-IQGAP1 as a biogenic microvesicles using proteomics and molecular biology [48]. IQGAP1, a scaffold protein, binds directly to GLS1 and mediates the secretion of GLS1 microvesicles. In addition, studies on breast cancer have found that trastuzumab resistance is related to CDC42 activation [64, 65]. Rho GTPases promote or inhibit NF- κ B pathway activation [49]. A relationship between CDC42 and NF- κ B p65 had not yet been reported, however, we found that CDC42 regulated NF- κ B p65 activation. Meanwhile, NF- κ B p65 can regulate GLS1 expression, which is consistent with previous reports. We predicted that NF- κ B p65 could act as a transcriptional regulator of GLS1 through an online database, and further ChIP experiments confirmed our conjecture. In summary, we propose that CDC42 regulates GLS1 expression through the NF- κ B P65 signaling pathway and regulates GLS1 microvesicle secretion through IQGAP1.

Mathematical models have been widely used in cancer treatment. However, there are limited mathematical models for trastuzumab studies, and the only available model was based on the response of subcutaneous tumors to trastuzumab treatment in mice with breast cancer [66]. Tumor microenvironment is a dynamic, evolving, complex, and heterogeneous microenvironment that is closely related to tumor progression and metastasis. Therefore, it is difficult to quantify the impact of individual factors in the tumor microenvironment from a monadic perspective. Thus, we proposed a mathematical model based on the mechanism of trastuzumab resistance, all while covering multiple scales in the tumor microenvironment, including tissue, molecular, cellular, and metabolic scales. The

interaction between these different scales was described using mathematical formula. We simulated the process of tumor growth, drug resistance, while combining combined treatment by adjusting parameters, and visualizing and quantifying the important factors of the microenvironment, showing the dynamic changes in tumors, blood vessels, macrophages, cytokines, and metabolites. The ABM confirmed that combination treatment of anti-glutamine metabolic therapy, anti-angiogenesis therapy and pro-M1 polarization had the most significant effect in reversing trastuzumab resistance. In the future, changing the model coefficients to present individual heterogeneity and introducing pharmacokinetics into the model is expected to provide guidance for the precise treatment of trastuzumab-resistant patients.

Currently, there is a lack of treatment guidelines to manage trastuzumab resistance in clinical practice. Paclitaxel, irinotecan, and other chemotherapy drugs are mainly used as second-line treatment. Several basic and clinical trials have shown that targeting tumor-dependent glutamine metabolism can effectively inhibit tumor growth [20, 56, 57]. Inhibitors of glutamine metabolism therapy are gradually being developed. The latest generation of CB839 has passed phase I/II clinical trials, which is expected to bring new hope and breakthrough for future cancer treatment [21, 22]. There is increasing evidence that TAM contribute to antitumor drug resistance, and studies investigating drugs that could block tumor progression by depolarizing the M2 phenotype of TAM in patients with various solid tumors are also being developed [67, 68]. Based on the REGARD and RAINBOW studies, the anti-angiogenesis drug ramucirumab is approved as a second-line treatment for advanced gastric cancer [69, 70]. In conclusion, the anti-glutamine metabolism, anti-angiogenesis, and M1 polarization therapy involved in this study have great prospects in future clinical applications, and are expected to overcome trastuzumab resistance in the form of combination therapy and become the first-line treatment of HER2-positive advanced gastric cancer.

Our study had some limitations. Due to the lack of recognized murine-derived gastric cancer cell lines and spontaneous gastric cancer models, our study relied on xenograft tumor assays in immune-deficient mice. It is difficult to draw conclusions about their functions in an immune-deficient background. Another limitation was that the transplantation assays were subcutaneous and not orthotopic. Organ specificity plays a crucial role in the immune response. The recognized murine gastric cancer cell lines were isolated and transgenic, and auto-neogenic mouse models were constructed. More animal models based on patient tissue sources should be developed in the future to promote scientific research concerning this topic.

5 | CONCLUSIONS

Taken together, our results suggest that tumor cell promotes glutamine metabolism, M2 phenotype polarization, and pro-angiogenic function of macrophage, which may contribute to acquired trastuzumab resistance in HER2-positive gastric cancer. Mechanistically, CDC42 activates NF- κ B p65 to regulate GLS1 expression and drives GLS1 microvesicle secretion via IQGAP1. Finally, a mathematical model was constructed to strategically select combinations of anti-glutamine metabolism, anti-angiogenesis, and pro-M1 polarization therapy to provide new insights into reversing trastuzumab resistance.

DECLARATIONS

AUTHORS CONTRIBUTIONS

Xingbin Hu, Zhenfeng Ma, Beibei Xu, Fenghua Wang and Min Shi designed the study, drafted and revised the manuscript. Xingbin Hu, Zhenfeng Ma, Zhiqi Yao, Bishan Liang and Jiao Wang performed all the experiments and statistical analyses. Shulong Li, Beibei Xu and Xingbin Hu designed the ABM. Wangjun Liao, Li Lin, Chunling Wang and Fenghua Wang provided samples and data of HER2-positive gastric cancer patients. Qijing Wu and Qiong Huang performed the data collection. Siting Zheng and Le Yu contributed to interpretation of clinical data. All these works were planned and supervised by Min Shi. All authors have read and approved the final manuscript.

ACKNOWLEDGEMENTS

The authors have nothing to report.

CONFLICT OF INTEREST STATEMENT

The authors declare that they have no competing interests.

CONSENT FOR PUBLICATION

Not applicable.

DATA AVAILABILITY STATEMENT

The data that supports the findings of this study could be available from the corresponding author upon reasonable request.

ETHICS APPROVAL AND CONSENT TO PARTICIPATE

Animal experimental procedures in this work were authorized by the Animal Care and Use Committee of Nanfang Hospital, Southern Medical University (NFYY-2021-0516) and followed the guidelines of the Laboratory Animal Centre of Southern Medical University. Clinical studies in this paper were approved by the Nanfang Hospital Ethics Review Board and conformed to International Eth-

ical Guidelines for Biomedical Research Involving Human Subjects and all participants signed an Informed Consent Form (NFEC-202001-K2).

ORCID

Wangjun Liao  <https://orcid.org/0000-0002-1364-8442>

Fenghua Wang  <https://orcid.org/0000-0003-1016-6867>

Min Shi  <https://orcid.org/0000-0003-0113-4089>

REFERENCES

- Sung H, Ferlay J, Siegel RL, Laversanne M, Soerjomataram I, Jemal A, et al. Global Cancer Statistics 2020: GLOBOCAN Estimates of Incidence and Mortality Worldwide for 36 Cancers in 185 Countries. *CA Cancer J Clin.* 2021;71(3):209–49.
- Allemani C, Matsuda T, Di Carlo V, Harewood R, Matz M, Niksic M, et al. Global surveillance of trends in cancer survival 2000–14 (CONCORD-3): analysis of individual records for 37 513 025 patients diagnosed with one of 18 cancers from 322 population-based registries in 71 countries. *Lancet.* 2018;391(10125):1023–75.
- Joshi SS, Badgwell BD. Current treatment and recent progress in gastric cancer. *CA Cancer J Clin.* 2021;71(3):264–79.
- Bang YJ, Van Cutsem E, Feyereislova A, Chung HC, Shen L, Sawaki A, et al. Trastuzumab in combination with chemotherapy versus chemotherapy alone for treatment of HER2-positive advanced gastric or gastro-oesophageal junction cancer (ToGA): a phase 3, open-label, randomised controlled trial. *Lancet.* 2010;376(9742):687–97.
- Gambardella V, Fleitas T, Tarazona N, Cejalvo JM, Gimeno-Valiente F, Martinez-Ciarpaglini C, et al. Towards precision oncology for HER2 blockade in gastroesophageal adenocarcinoma. *Ann Oncol.* 2019;30(8):1254–64.
- Wang FH, Zhang XT, Li YF, Tang L, Qu XJ, Ying JE, et al. The Chinese Society of Clinical Oncology (CSCO): Clinical guidelines for the diagnosis and treatment of gastric cancer, 2021. *Cancer Commun (Lond).* 2021;41(8):747–95.
- Piro G, Carbone C, Cataldo I, Di Nicolantonio F, Giacopuzzi S, Aprile G, et al. An FGFR3 Autocrine Loop Sustains Acquired Resistance to Trastuzumab in Gastric Cancer Patients. *Clin Cancer Res.* 2016;22(24):6164–75.
- Berns K, Horlings HM, Hennessy BT, Madiredjo M, Hijmans EM, Beelen K, et al. A functional genetic approach identifies the PI3K pathway as a major determinant of trastuzumab resistance in breast cancer. *Cancer Cell.* 2007;12(4):395–402.
- Pohlmann PR, Mayer IA, Mernaugh R. Resistance to Trastuzumab in Breast Cancer. *Clin Cancer Res.* 2009;15(24):7479–91.
- Narayan M, Wilken JA, Harris LN, Baron AT, Kimbler KD, Maihle NJ. Trastuzumab-induced HER reprogramming in “resistant” breast carcinoma cells. *Cancer Res.* 2009;69(6):2191–4.
- Renner K, Singer K, Koehl GE, Geissler EK, Peter K, Siska PJ, et al. Metabolic Hallmarks of Tumor and Immune Cells in the Tumor Microenvironment. *Front Immunol.* 2017;8:248.
- Sung JY, Cheong JH. Intercellular communications and metabolic reprogramming as new predictive markers for immunotherapy responses in gastric cancer. *Cancer Commun (Lond).* 2022;42(6):572–5.

13. Zhao Y, Liu H, Liu Z, Ding Y, Ledoux SP, Wilson GL, et al. Overcoming trastuzumab resistance in breast cancer by targeting dysregulated glucose metabolism. *Cancer Res.* 2011;71(13):4585–97.
14. Wang J, Huang Q, Hu X, Zhang S, Jiang Y, Yao G, et al. Disrupting circadian rhythm via the PER1-HK2 axis reverses trastuzumab resistance in gastric cancer. *Cancer Res.* 2022;82(8):1503–1517.
15. Sethunath V, Hu H, De Angelis C, Veeraghavan J, Qin L, Wang N, et al. Targeting the Mevalonate Pathway to Overcome Acquired Anti-HER2 Treatment Resistance in Breast Cancer. *Mol Cancer Res.* 2019;17(11):2318–30.
16. Kim JH, Lee KJ, Seo Y, Kwon JH, Yoon JP, Kang JY, et al. Effects of metformin on colorectal cancer stem cells depend on alterations in glutamine metabolism. *Sci Rep.* 2018;8(1):409.
17. Jiang ZF, Wang M, Xu JL, Ning YJ. Hypoxia promotes mitochondrial glutamine metabolism through HIF1 α -GDH pathway in human lung cancer cells. *Biochem Biophys Res Commun.* 2017;483(1):32–8.
18. Ko YH, Lin Z, Flomenberg N, Pestell RG, Howell A, Sotgia F, et al. Glutamine fuels a vicious cycle of autophagy in the tumor stroma and oxidative mitochondrial metabolism in epithelial cancer cells: implications for preventing chemotherapy resistance. *Cancer Biol Ther.* 2011;12(12):1085–97.
19. Kim S, Kim DH, Jung WH, Koo JS. Expression of glutamine metabolism-related proteins according to molecular subtype of breast cancer. *Endocr Relat Cancer.* 2013;20(3):339–48.
20. Katt WP, Lukey MJ, Cerione RA. A tale of two glutaminases: homologous enzymes with distinct roles in tumorigenesis. *Future Med Chem.* 2017;9(2):223–43.
21. Motzer RJ, Lee CH, Emamekhoo H, Matrana M, Percent I, Hsieh JJ, et al. ENTRATA: Randomized, double-blind, phase II study of telaglenastat (tela; CB-839) + everolimus (E) vs placebo (pbo) + E in patients (pts) with advanced/metastatic renal cell carcinoma (mRCC). *Annals of Oncology.* 2019;30:v889–v90.
22. Zhao Y, Feng X, Chen Y, Selfridge JE, Gorityala S, Du Z, et al. 5-Fluorouracil Enhances the Antitumor Activity of the Glutaminase Inhibitor CB-839 against PIK3CA-Mutant Colorectal Cancers. *Cancer Res.* 2020;80(21):4815–27.
23. Viola A, Munari F, Sanchez-Rodriguez R, Scolaro T, Castegna A. The Metabolic Signature of Macrophage Responses. *Front Immunol.* 2019;10:1462.
24. de Goede KE, Driessen AJM, van den Bossche J. Metabolic Cancer-Macrophage Crosstalk in the Tumor Microenvironment. *Biology (Basel).* 2020;9(11):380.
25. Wu JY, Huang TW, Hsieh YT, Wang YF, Yen CC, Lee GL, et al. Cancer-Derived Succinate Promotes Macrophage Polarization and Cancer Metastasis via Succinate Receptor. *Mol Cell.* 2020;77(2):213–27 e5.
26. Morrissey SM, Zhang F, Ding C, Montoya-Durango DE, Hu X, Yang C, et al. Tumor-derived exosomes drive immunosuppressive macrophages in a pre-metastatic niche through glycolytic dominant metabolic reprogramming. *Cell Metab.* 2021;33(10):2040–58 e10.
27. van Niel G, D'Angelo G, Raposo G. Shedding light on the cell biology of extracellular vesicles. *Nat Rev Mol Cell Biol.* 2018;19(4):213–28.
28. Antonyak MA, Wilson KF, Cerione RA. R(h)oads to microvesicles. *Small GTPases.* 2012;3(4):219–24.
29. Wu B, Huang Y, Braun AL, Tong Z, Zhao R, Li Y, et al. Glutaminase-containing microvesicles from HIV-1-infected macrophages and immune-activated microglia induce neurotoxicity. *Mol Neurodegener.* 2015;10:61.
30. Wolff AC, Hammond MEH, Allison KH, Harvey BE, Mangu PB, Bartlett JMS, et al. Human Epidermal Growth Factor Receptor 2 Testing in Breast Cancer: American Society of Clinical Oncology/College of American Pathologists Clinical Practice Guideline Focused Update. *J Clin Oncol.* 2018;36(20):2105–22.
31. Eisenhauer EA, Therasse P, Bogaerts J, Schwartz LH, Sargent D, Ford R, et al. New response evaluation criteria in solid tumours: revised RECIST guideline (version 1.1). *Eur J Cancer.* 2009;45(2):228–47.
32. Kanehisa M, Furumichi M, Tanabe M, Sato Y, Morishima K. KEGG: new perspectives on genomes, pathways, diseases and drugs. *Nucleic Acids Res.* 2017;45(D1):D353–D61.
33. Gong Y, Ji P, Yang YS, Xie S, Yu TJ, Xiao Y, et al. Metabolic-Pathway-Based Subtyping of Triple-Negative Breast Cancer Reveals Potential Therapeutic Targets. *Cell Metab.* 2021;33(1):51–64 e9.
34. Hanzelmann S, Castelo R, Guinney J. GSEA: gene set variation analysis for microarray and RNA-seq data. *BMC Bioinformatics.* 2013;14:7.
35. Ritchie ME, Phipson B, Wu D, Hu Y, Law CW, Shi W, et al. limma powers differential expression analyses for RNA-sequencing and microarray studies. *Nucleic Acids Res.* 2015;43(7):e47.
36. Yu G, Wang LG, Han Y, He QY. clusterProfiler: an R package for comparing biological themes among gene clusters. *OMICS.* 2012;16(5):284–7.
37. Ali HR, Chlon L, Pharoah PD, Markowitz F, Caldas C. Patterns of Immune Infiltration in Breast Cancer and Their Clinical Implications: A Gene-Expression-Based Retrospective Study. *PLoS Med.* 2016;13(12):e1002194.
38. Newman AM, Liu CL, Green MR, Gentles AJ, Feng W, Xu Y, et al. Robust enumeration of cell subsets from tissue expression profiles. *Nat Methods.* 2015;12(5):453–7.
39. Donahue DA, Kaufman LE, Avalos J, Simion FA, Cerven DR. Survey of ocular irritation predictive capacity using Chorioallantoic Membrane Vascular Assay (CAMVA) and Bovine Corneal Opacity and Permeability (BCOP) test historical data for 319 personal care products over fourteen years. *Toxicol In Vitro.* 2011;25(2):563–72.
40. Merckx G, Tay H, Lo Monaco M, van Zandvoort M, De Spiegelaere W, Lambrichts I, et al. Chorioallantoic Membrane Assay as Model for Angiogenesis in Tissue Engineering: Focus on Stem Cells. *Tissue Eng Part B Rev.* 2020;26(6):519–39.
41. Dusoswa SA, Horrevorts SK, Ambrosini M, Kalay H, Paauw NJ, Nieuwland R, et al. Glycan modification of glioblastoma-derived extracellular vesicles enhances receptor-mediated targeting of dendritic cells. *J Extracell Vesicles.* 2019;8(1):1648995.
42. Wang Z, Butner JD, Kerketta R, Cristini V, Deisboeck TS. Simulating cancer growth with multiscale agent-based modeling. *Semin Cancer Biol.* 2015;30:70–8.
43. Sun X, Zhang L, Tan H, Bao J, Strouthos C, Zhou X. Multiscale agent-based brain cancer modeling and prediction of TKI treatment response: incorporating EGFR signaling pathway and angiogenesis. *BMC Bioinformatics.* 2012;13:218.

44. Mahlbacher G, Curtis LT, Lowengrub J, Frieboes HB. Mathematical modeling of tumor-associated macrophage interactions with the cancer microenvironment. *J Immunother Cancer*. 2018;6(1):10.
45. Chen Y, Song Y, Du W, Gong L, Chang H, Zou Z. Tumor-associated macrophages: an accomplice in solid tumor progression. *J Biomed Sci*. 2019;26(1):78.
46. Muralidharan-Chari V, Clancy JW, Sedgwick A, D'Souza-Schorey C. Microvesicles: mediators of extracellular communication during cancer progression. *J Cell Sci*. 2010;123(Pt 10):1603–11.
47. Antonyak MA, Li B, Boroughs LK, Johnson JL, Druso JE, Bryant KL, et al. Cancer cell-derived microvesicles induce transformation by transferring tissue transglutaminase and fibronectin to recipient cells. *Proc Natl Acad Sci U S A*. 2011;108(12):4852–7.
48. Wang J, Zhuang X, Greene KS, Si H, Antonyak MA, Druso JE, et al. Cdc42 functions as a regulatory node for tumour-derived microvesicle biogenesis. *J Extracell Vesicles*. 2021;10(3):e12051.
49. Tong L, Tergaonkar V. Rho protein GTPases and their interactions with NFκB: crossroads of inflammation and matrix biology. *Biosci Rep*. 2014;34(3):e00115.
50. White CD, Brown MD, Sacks DB. IQGAPs in cancer: a family of scaffold proteins underlying tumorigenesis. *FEBS Lett*. 2009;583(12):1817–24.
51. Birladeanu AM, Rogalska M, Potiri M, Papadaki V, Andreadou M, Kontoyiannis DL, et al. The scaffold protein IQGAP1 links heat-induced stress signals to alternative splicing regulation in gastric cancer cells. *Oncogene*. 2021;40(36):5518–32.
52. Cline MS, Craft B, Swatloski T, Goldman M, Ma S, Haussler D, et al. Exploring TCGA Pan-Cancer data at the UCSC. *Cancer Genomics Browser*. *Sci Rep*. 2013;3:2652.
53. Qie S, Chu C, Li W, Wang C, Sang N. ErbB2 activation upregulates glutaminase 1 expression which promotes breast cancer cell proliferation. *J Cell Biochem*. 2014;115(3):498–509.
54. Fu A, Yu Z, Song Y, Zhang E. Silencing of glutaminase 1 resensitizes Taxol-resistant breast cancer cells to Taxol. *Mol Med Rep*. 2015;11(6):4727–33.
55. Lu WQ, Hu YY, Lin XP, Fan W. Knockdown of PKM2 and GLS1 expression can significantly reverse oxaliplatin-resistance in colorectal cancer cells. *Oncotarget*. 2017;8(27):44171–85.
56. Leone RD, Zhao L, Englert JM, Sun IM, Oh MH, Sun IH, et al. Glutamine blockade induces divergent metabolic programs to overcome tumor immune evasion. *Science*. 2019;366(6468):1013–21.
57. Oh MH, Sun IH, Zhao L, Leone RD, Sun IM, Xu W, et al. Targeting glutamine metabolism enhances tumor-specific immunity by modulating suppressive myeloid cells. *J Clin Invest*. 2020;130(7):3865–84.
58. Sica A, Schioppa T, Mantovani A, Allavena P. Tumour-associated macrophages are a distinct M2 polarised population promoting tumour progression: potential targets of anti-cancer therapy. *Eur J Cancer*. 2006;42(6):717–27.
59. Bloom MJ, Jarrett AM, Triplett TA, Syed AK, Davis T, Yankeelov TE, et al. Anti-HER2 induced myeloid cell alterations correspond with increasing vascular maturation in a murine model of HER2+ breast cancer. *BMC Cancer*. 2020;20(1):359.
60. Upton R, Banuelos A, Feng D, Biswas T, Kao K, McKenna K, et al. Combining CD47 blockade with trastuzumab eliminates HER2-positive breast cancer cells and overcomes trastuzumab tolerance. *Proc Natl Acad Sci U S A*. 2021;118(29):e2026849118.
61. Dehne N, Mora J, Namgaladze D, Weigert A, Brune B. Cancer cell and macrophage cross-talk in the tumor microenvironment. *Curr Opin Pharmacol*. 2017;35:12–9.
62. Wu B, Liu J, Zhao R, Li Y, Peer J, Braun AL, et al. Glutaminase 1 regulates the release of extracellular vesicles during neuroinflammation through key metabolic intermediate alpha-ketoglutarate. *J Neuroinflammation*. 2018;15(1):79.
63. Li B, Antonyak MA, Zhang J, Cerione RA. RhoA triggers a specific signaling pathway that generates transforming microvesicles in cancer cells. *Oncogene*. 2012;31(45):4740–9.
64. Johnson E, Seachrist DD, DeLeon-Rodriguez CM, Lozada KL, Miedler J, Abdul-Karim FW, et al. HER2/ErbB2-induced breast cancer cell migration and invasion require p120 catenin activation of Rac1 and Cdc42. *J Biol Chem*. 2010;285(38):29491–501.
65. Zhang Y, Li J, Lai XN, Jiao XQ, Xiong JP, Xiong LX. Focus on Cdc42 in Breast Cancer: New Insights, Target Therapy Development and Non-Coding RNAs. *Cells*. 2019;8(2):146.
66. Jarrett AM, Bloom MJ, Godfrey W, Syed AK, Ekrut DA, Ehrlich LI, et al. Mathematical modelling of trastuzumab-induced immune response in an in vivo murine model of HER2+ breast cancer. *Math Med Biol*. 2019;36(3):381–410.
67. Escamilla J, Schokrpur S, Liu C, Priceman SJ, Moughon D, Jiang Z, et al. CSF1 receptor targeting in prostate cancer reverses macrophage-mediated resistance to androgen blockade therapy. *Cancer Res*. 2015;75(6):950–62.
68. Shiao SL, Ruffell B, DeNardo DG, Faddegon BA, Park CC, Coussens LM. TH2-Polarized CD4(+) T Cells and Macrophages Limit Efficacy of Radiotherapy. *Cancer Immunol Res*. 2015;3(5):518–25.
69. Fuchs CS, Tomasek J, Yong CJ, Dumitru F, Passalacqua R, Goswami C, et al. Ramucirumab monotherapy for previously treated advanced gastric or gastro-oesophageal junction adenocarcinoma (REGARD): an international, randomised, multicentre, placebo-controlled, phase 3 trial. *Lancet*. 2014;383(9911):31–9.
70. Wilke H, Muro K, Van Cutsem E, Oh SC, Bodoky G, Shimada Y, et al. Ramucirumab plus paclitaxel versus placebo plus paclitaxel in patients with previously treated advanced gastric or gastro-oesophageal junction adenocarcinoma (RAINBOW): a double-blind, randomised phase 3 trial. *Lancet Oncol*. 2014;15(11):1224–35.

SUPPORTING INFORMATION

Additional supporting information can be found online in the Supporting Information section at the end of this article.

How to cite this article: Hu X, Ma Z, Xu B, Li S, Yao Z, Liang B, et al. Glutamine metabolic microenvironment drives M2 macrophage polarization to mediate trastuzumab resistance in HER2-positive gastric cancer. *Cancer Commun*. 2023;43:909–937. <https://doi.org/10.1002/cac2.12459>